Aalto-yliopisto
Aalto-universitetet
Aalto University

Master's Programme in Geoengineering

The use of Gaussian splatting for 3D digitization for rock mass characterization and visualization

---

Stephen Okutu-Ayiku

Master's thesis
2025

Aalto-yliopisto
Aalto-universitetet
Aalto University

Author Okutu-Ayiku Stephen Adi

Title of thesis The use of Gaussian splatting for 3D digitization for rock mass characterization and visualization

Programme Master's Programme in Geoengineering

Thesis supervisor Prof. Mikael Rinne

Thesis advisor(s) Dr. Mateusz Janiszewski

Date 23.11.2025
Number of pages 62+6
Language English

Abstract

This study evaluates the potential of 3D Gaussian Splatting (3DGS) as a novel 3D digitization method for rock mass characterization. The main focus was on the relative accuracy of 3DGS, its efficiency, and visualization capabilities compared to the traditional photogrammetric methods and manual field methods. Gaussian Splatting generally enables the creation of real-time, photo-realistic 3D reconstructions through a point-based rendering technique that blends both geometry and texture data. This research investigated optimal data acquisition and processing workflows, the influence of device capabilities (mobile versus desktop), and the applicability of 3DGS under challenging underground conditions.

Using datasets obtained from the Underground Research Laboratory of Aalto University (URLA), models of 3D Gaussian splatting were made with Jawset Postshot software and geometrically compared to mesh-based photogrammetry and point cloud-based photogrammetry. Rock Quality Designation (RQD) measurements were extracted digitally with the three methods and compared with the manual/physical scanline measurements to assess geometric accuracy. Statistical analyses, including correlation coefficients and Root Mean Square Error (RMSE), were used to quantify accuracy among the different techniques.

Results indicate that 3D Gaussian Splatting achieved a higher correlation with the physical measurements compared to the mesh-based photogrammetric method, and a subsequent lower RMSE to the mesh-based photogrammetric methods using the point cloud-based photogrammetry as reference. These results, therefore, showed the superior geometric fidelity of 3DGS to the mesh-based photogrammetric methods. Visual quality assessment by human participants also showed that Gaussian Splatting produced sharper, more complete, and colour-accurate representations. Although specular reflections and low-light noise presented challenges, 3DGS still outperformed traditional mesh-based photogrammetry in measurement consistency. These findings highlight 3D Gaussian Splatting as a promising tool for rapid, accurate, and interactive rock mass documentation and analysis in underground engineering applications.

Table of contents

List of Figures

List of Tables

Preface and acknowledgements

I would like to warmly thank Professor Mikael Rinne for his guidance, encouragement, and support throughout this thesis. The monthly presentation of the thesis progression kept me on my toes throughout this this, his insights and detailed feedback on every document have been just invaluable.

I am also eternally grateful to Dr. Mateusz Janiszewski for his dedicated supervision and practical guidance. From the beginning, his comments and advice greatly fortified the direction of the work and helped me stay on the right track.

Thank you both for your support during this process.

Otaniemi, 20 November 2022
Okutu-Ayiku Stephen

Symbols and abbreviations

Abbreviations

RMR	Rock Mass Rating
RQD	Rock Quality Designation
UCS	Uniaxial Compressive Strength
Js	Joint and bedding spacing
SfM	Structure from Motion
SfM-MVS	Structure-from-motion Multi-view Stereo
LiDAR	light detection and ranging
UAV	unmanned aerial vehicle
Po	Postshot
CC	CloudCompare
Phy	Physical
RC	Reality Capture
AD	Absolute Difference
SoD	Square of Difference
3DGS	3D Gaussian Splatting
m	meters

1 INTRODUCTION

1.1 Background Of Study

With the advance in computer programming, from large language models to neural networks, the quality of rendering has also seen significant improvement with the invention of radiance field methods. Characterizing rock mass has evolved significantly from traditional geological mapping methods. In the past, researchers relied heavily on manual measurements and physical interaction with rock surfaces, which often introduced subjectivity and inefficiencies into the process. The advent of photogrammetry revolutionized the field by enabling the creation of digital 3D models from photographic images, offering a faster and less biased approach while eliminating the need for physical contact.

The rock engineering discipline has already been active in the use of photogrammetry to safely and accurately characterize rock masses for decades now. This makes the discipline invested in trying new rendering techniques and researching possibilities for improving efficiency and accuracy of characterizing rock masses, especially in inaccessible or hazardous environments. The existing techniques in photogrammetry and remote sensing, although capable of showing 3D rendering of the rock surfaces, the techniques often have challenges with producing very detailed 3D reconstructions. It always loses some fine details of the rock surface because of the limitations of the method. For example, presence of specular reflections on a rock surface which may result in distorted renderings in the traditional photogrammetric methods can be the difference between the ability to visualize water on the rock surface or not. As noted by Calantropio & Chiabrando (2024), reflections from water creates difficulties in feature identification using photogrammetry.

Although the first radiance field method, Neural Radiance Field (NeRF) provides a better solution to the visualization problem, this method is computationally demanding and has very long training times when generating a neural render or 3D mesh. It presents another challenge to engineering constructions which demand fast analysis to determine which actions to take before catastrophic damage in the construction occurs (Remondino et al., 2023).

To address these limitations, this study aims to make an effort in applying the novel 3D Gaussian splatting method which has demonstrated faster training times and enhanced image clarity in other fields of image rendering in rock engineering to evaluate its usability and accuracy. This research will focus on providing real-time rendering solutions for more precise and accurate mapping results for rock characterization.

1.2 Goals and Objectives

The primary aim of this research is to evaluate the potential of Gaussian splatting for rock mass characterization.
Specific objectives include:

- Establishing the methodology for the application of Gaussian Splatting in rock engineering applications.
- Comparing the geometrical validity of Gaussian splatting, photogrammetry, and traditional mapping techniques.
- Comparing the measurement consistency across multiple 3D Gaussian splatting software applications.
- Assessing how device capabilities (between mobile and desktop) affect the quality and accuracy of Gaussian splatting outputs.

1.3 Research questions

This study seeks to evaluate the usability, accuracy and efficiency of 3D Gaussian Splatting in rock engineering. To achieve this, the research will address the following questions:

1. What are the optimal data acquisition workflows, software tools and processing parameters required to generate high-quality Gaussian splats in underground tunnel conditions?
2. How can geometric measurements be accurately and consistently extracted from Gaussian splatting visualizations?
3. How accurate and reliable are the rock quality designation values derived from 3D gaussian splatting models compared to traditional photogrammetry and manual field measurements?
4. How consistent are the geometrical distance measurements across different Gaussian splatting software toolchains?
5. Can smartphones provide reliable measurement and visualization quality for rock mass characterization using Gaussian splatting compared to desktop-based systems?

1.4 Scope of study

This study focuses on evaluating the effectiveness of 3D Gaussian splatting (3DGS) in rock mass characterization, specifically in its geometrical accuracy. The research compares 3DGS and traditional photogrammetry in terms of accuracy, speed of rendering and visualization quality. It investigates the ability of 3DGS to preserve fine surface details like fractures and water-induced reflections.

The study is limited to 3D rendering techniques and may not include physical rock sample analysis or chemical and mineralogical assessments. It is

conducted in a research location with trusted data from geological experts so that accuracy in measurements is easily compared. Although effectiveness in hazardous and inaccessible environments is a major focus, external environmental factors like dust pollution and lighting variations are not explicitly considered in this analysis. Also, the computational demands and speed of rendering of Neural Radiance Fields (NeRFs) is not researched in this research due to time constraints.

The objective to define the strengths and limitations of 3DGS in rock characterization by this research is to contribute to quicker, more accurate, and computationally efficient rendering solutions in rock assessments.

1.5 Structure of study

This study is organized into five chapters, each covering essential aspects of the research:

Chapter 1: Introduction

This chapter introduces the research by providing the background of the study, research objectives, research questions, and scope of the study. It establishes the foundation for the research and highlights its significance.

Chapter 2: Literature Review

This chapter presents brief review of existing research on rock mass characterization, photogrammetry, Neural Radiance Fields (NeRFs), and 3D Gaussian Splatting (3DGS). It also explores how advancements in technology have influenced current engineering methods.

Chapter 3: Methodology

This chapter describes the research approach, data sources, and computational techniques used in the study. It details the implementation of 3DGS, along with the comparative methods and evaluation metrics employed for analysis.

Chapter 4: Results and Discussion

This chapter presents the findings of the study, including a comparative analysis of 3DGS, and photogrammetry. It discusses the strengths and limitations of each method, focusing on real-time rendering performance and geometric accuracy.

Chapter 5: Conclusion and Recommendations

The final chapter summarizes the key findings of the study, discusses their implications for rock engineering, and provides recommendations for future research and potential practical applications.

2 LITERATURE REVIEW

2.1 Rocks and its construction methods

Rocks are defined as these naturally formed inorganic, crystalline minerals with distinct physical and chemical characteristics (Rangel-Buitrago et al., 2024). Rocks have played a key role in satisfying the human (and sometimes even animal) basic need of shelter provision, it has always been an important part of human history from the prehistoric ages when men used to live in caves, using the whole rock material as accommodation and when these prehistoric ancestors made primitive tools for building, hunting and warfare from rocks (Yazarı et al., 2017).

Humans often appreciated the use of these materials due to the unique properties they possess. Their durability, strength, resistance to weathering, erosion, fire, and decay. These properties are all evident looking into some of the long-standing ancient stone structures such as the Pyramids of Giza and the Colosseum. Furthermore, the availability of rocks is usually not confined to a specific geological location, the lithosphere is made up of hundreds of kilometres of rocks everywhere.

2.2 Manual mapping techniques

Geological information is a core aspect in rock mechanics, essential for defining rock types, structural discontinuities, and material properties in the rock mass. The main methods for collecting these geological data (i.e. core logging and the field mapping) have been the same since the inception of this discipline even amidst the huge advancements in technology and equipment. These methods are heavily dependent on discontinuity finding within a rock mass and the estimation of how the quantity, type and properties of the discontinuities will contribute to the characteristics of the rock mass.

A discontinuity as defined by(Sultan Shah et al., 2022) is a mechanical break or plane of weakness in a rock mass. These planes exhibit different physically or chemically characteristics from the surrounding rock (Kumar Singh et al., 2023) and have a major impact on the rock mass strength, permeability, and slope stability (Herrero et al., 2022). The discontinuities of a rock mass during fieldwork are detected by mapping the rock. This involves measuring and locating the orientation of the discontinuities and other geological features with a compass. The main measured categories of geological features are either planar or linear, the linear structures are determined by trend and plunge, whereas the planar structures (bedding planes and faults) are inferred by measuring strike, dip, and dip directions (Kissi-Ameyaw et al., 2020). For the measurements, the most used compasses for geological mapping in the field currently are the Brunton and Silver compasses

(Kimberly Schulte, 2021), due to their integrated clinometer features for measuring vertical angles (Steven Earle, 2019). They are capable of measuring all the feature found in a rock, including the geometry of joints, bedding planes, metamorphic foliations, and lineation (Kimberly Schulte, 2021).

2.3 The various rock mass characterization methods used

A detailed characterization of discontinuities is essential for understanding how the rock mass behaves and to ensure the stability of engineering projects. Traditionally, rock mass characterization relied on direct field measurements of discontinuity planes, such as joints, faults, bedding planes, and foliations. These measurements involved determining orientation (dip and dip direction), spacing, and persistence, which were then analyzed using stereographic projections to identify dominant discontinuity sets. The technique employed frequently relied on the researcher's experience and familiarity with the local conditions (Thambidurai N Singh, 2023).

The most used rock mass classification systems: Rock Mass Rating (RMR), the Geological Strength Index (GSI), and the Rock Tunnel Quality Index (Q-system), all share the same aim of quantifying rock masses and assessing their stability. The systems rely heavily on the frequency, distribution, and characteristics of discontinuities, which significantly impact mechanical and hydraulic rock properties (Gottron & Henk, 2021; Kumar Singh et al., 2023). For example, the Q-system which was specifically designed for tunnels incorporates six parameters: rock quality designation (RQD), degree of joint alteration and clay filling, number of joint sets, joint roughness, water input, and the stress reduction factor. Similarly, the RMR index considers rock uniaxial compressive strength (UCS), RQD, joint and bedding spacing (JS), joint condition, groundwater condition, and discontinuity orientation relative to tunnel openings (Kumar Singh et al., 2023). Furthermore, the Geological Strength Index (GSI), originally proposed by Hoek and Brown, has evolved from a qualitative index into a quantitative classification system, incorporating rock block geometry and joint surface conditions such as weathering, roughness, and infilling (Kumar Singh et al., 2023).

When it comes to rock mass fracturing, the Rock Quality Designation (RQD) parameter, which measures the proportion of intact rock core segments longer than 10 cm is the main parameter among all the systems. While RQD is often determined through direct core measurements, it can also be estimated using empirical formulas and statistical distribution functions based on available geological data if required (Gottron & Henk, 2021)(Deere D.U, 1964)

Due to the importance of discontinuity assessments in rock mass characterization, traditional field survey methods have been concluded to be time-consuming, hazardous, and prone to human error, especially in geohazard-

prone areas or inaccessible terrains and this seems to be a big limitation to its application (Deheng Kong et al., 2021). Additionally, the manual data collection normally lack precision, as its accuracy depends heavily on the precision, measurement skills and experience of geologists (Deheng Kong et al., 2021). Kissi-Ameyaw et al., (2020) argues that the traditional method of collecting these geological data has also not been a good use of the collector's time and energy. The use of more sophisticated equipment which we now have could better facilitate this process.

2.4 Evolution into digital techniques and laser scanning

In recent years, technologies like smartphones, small unmanned aerial vehicles (UAVs), aircrafts and satellites have revolutionized the way we collect structural measurements in the field. Immediate data collection has been made possible by these remote sensing tools, also enabling data redundancy and uncertainty estimations (Cicilie Trede1 et al., 2019). When it comes to electronic storage, displaying, querying, and analysis of rock geometry and characteristics, Geographic Information System (GIS) software and tools which have been used within the past 10 to 20 years demonstrates an overwhelming improvement in its application of geological mapping.

The developments in remote sensing methods for geotechnical surveys, including digital photogrammetry and light detection and ranging (LiDAR, airborne and terrestrial laser scanning), have made it possible to obtain high-resolution, georeferenced 3D information of discontinuities to aid in the characterization of rock mass. Researchers can consequently use integrated mathematical methods to extract geological properties from the virtual geometry of terrains and rock faces created by 3D point clouds (Deheng Kong et al., 2021). The application of this recent development is termed photogrammetry, and it has resulted in many studies developing semi-automated extraction and characterization of discontinuities based on analyses of 3D point clouds, which are frequently used in non-contact surveys like Laser Imaging or LiDAR. The use of these newer techniques offers amazing possibilities to accuracy such that even the International Society for Rock Mechanics and Rock Engineering has recommended photogrammetry to measure discontinuity (Herrero et al., 2022). For instance, laser scanning techniques have been explored to be capable of comparatively improving the measurement of joint aperture, roughness, infilling, weathering, and enhancing the reliability of discontinuity characterization in general (Kumar Singh et al., 2023).

2.5 Photogrammetry from structure from motion (SfM)

Photogrammetry is a measurement technique that is used to extract the geometry, displacement, and deformation of a structure using photographs or digital images. The concept of photogrammetry is fundamentally related to perspective concept which goes back all the way to Leonardo da Vinci (Baqersad et al., 2017). In its early days as measurement technique, photogrammetry was used for aerial and terrestrial applications largely motivated by military reconnaissance, but with the advances in digital cameras and the ability to buy low-cost, high-resolution cameras, the applications expanded to include other branches of science such as civil and mechanical engineering. Researchers have coined various terms like close-range photogrammetry, videogrammetry, dynamic photogrammetry, computer vision, machine vision, and robot vision to refer to different modes and processes of this measurement technique (Baqersad et al., 2017).

Photogrammetric methods like Structure-from-motion Multi-view Stereo (SfM-MVS) have found a great applicability Rock Mechanics by digitizing the rock mass surface and extracting discontinuities using computer-assisted mapping methods (Janiszewski et al., 2023). Using Unmanned aerial vehicle (UAV) in photogrammetry, integrated with structure from motion (SfM) technique actually offers a low-budget, lightweight, timesaving, and user-friendly remote sensing alternative to manual compass measurements, and is increasing in interest and application throughout geosciences and rock engineering. The Structure from Motion (SfM) technique involves a series of computer vision algorithms (e.g., feature detection, bundle adjustment, and point cloud generation) that provides a technically more feasible solution for 3D surface reconstruction (Deheng Kong et al., 2021).

The term Structure from motion (SfM) as originally coined by (Ullman, (1979) is an advanced photogrammetric technique that has emerged from advances in computer vision and traditional photogrammetry, which utilizes a series of 2D images of an object, or a specific region obtained by a moving sensor as input to extract features and produce high-quality 3D structures (Deliry & Avdan, 2021). In geosciences application, it is used as a low-cost topographic survey technique to produce dense 3D point clouds, digital elevation models, and topographic maps however, in rock mechanics, the 3D point clouds generation is the most significant to acquire point cloud data for 3D characterization of structural planes in tunnels and outcrops (Chen et al., 2023). The commonest scene representations are ‘meshes’ and ‘points’ because of how well suited they are for quick GPU/CUDA based rasterization (making 2D pixels of 3D models and scenes to be displayed on a screen). SfM is used to reconstruct a sparse 3D point cloud model of the photographed object or scene, which is then refined to a denser and finer resolution by applying multi-view stereo (MVS) technique. In the computer vision literature, the full process is prevalently abbreviated as SfM, while the complete reconstruction is accomplished by performing an entire SfM–MVS workflow,

which employs multiple algorithms based on 3D computer vision, and photogrammetry techniques (Deliry & Avdan, 2021).

In the SfM process, the initial step is to extract the features and match them, then geometric verification comes next. Reconstruction is based on the resulting scene graph, which is seeded with a carefully chosen two-view reconstruction. The new images are then gradually registered, scene points are triangulated, outliers are filtered and finally bundle adjustment (BA) is used to refine the reconstruction (Schönberger & Frahm, 2016).

Photogrammetry as a tool has come a long way from only extracting rigid body displacements of objects or discrete points to collecting full-field information in rock characterization (Baqersad et al., 2017). A notable example from a study in (Davide et al., 2023)'s work shows how aerial photogrammetry was used to address the challenges in the inaccessible and hazardous terrain of the Cape Tindari promontory, where the geological and geomorphological conditions led to persistent rockfalls which posed risks to pedestrian pathways at the cliff base. It was nearly impossible to access the cliff for traditional rock mass survey due to its sub-vertical morphology and dense vegetation. Using the aerial photogrammetry, was employed to get high-resolution data over the large, unstable area, capturing up to millimeter scale details.

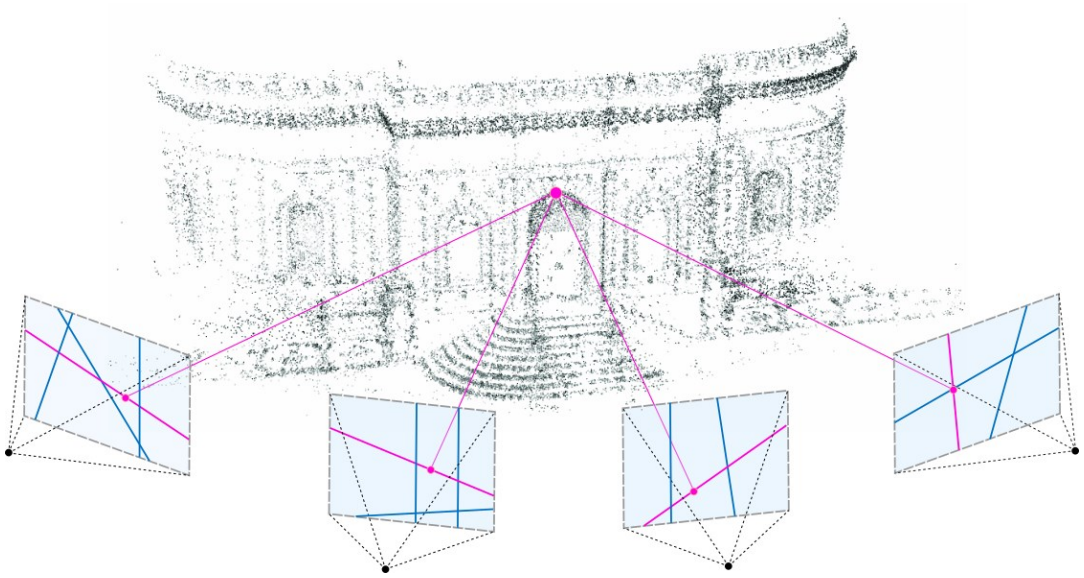

Figure 1. Generation of point clouds of a building using Structure from Motion from multiple camera angles. Source(Geppert et al., 2020) (Deliry & Avdan, 2021)

2.6 Rock mass characterization from 3D models

Efficient feature extraction from the processed data is one of the key components of employing 3D models for geological structure identification and quantification. Geologists and engineers can now see, measure, and examine

rock surfaces with previously unheard-of precision and repeatability due to advancements in 3D modeling techniques over the last 20 years. Currently available digital techniques for discontinuity mapping mostly use Structure-from-Motion (SfM) photogrammetry or LiDAR scanning to create dense 3D point clouds. These point clouds serve as preliminary data for further analysis since they represent an accurate geometric depiction of the relevant rock surfaces.

The process of determining and characterizing joints, fractures, and bedding planes is a key part of the feature extraction process from these point clouds. Each point's surface normal is calculated, enabling algorithms to find planar features that match structural discontinuities. In addition to orientation, other factors that are important for rock engineering and slope stability assessments are trace lengths, spacing, roughness, persistence, and block size of the discontinuities. Fine-scale surface textures are crucial for precise roughness and spacing measurements, and photogrammetry in particular is excellent at capturing these.

Rock surface properties like roughness, brightness, and texture, however, have an impact on how well discontinuity detection works and can change greatly throughout lithologies (Chen et al., 2023). The accuracy of feature extraction is frequently impacted by this fluctuation, particularly for surfaces that are highly uneven or subtle.

2.7 Radiance fields

Radiance-based modelling techniques are some of the advanced computational imaging solutions that has been specifically adapted to solve the issues presented by modelling highly uneven rock surfaces. These techniques enhance the identification and depiction of discontinuities in difficult-to-see situations by capturing intricate lighting interactions and deducing the material characteristics of the rock surfaces. By combining these modern imaging methods with conventional point cloud analysis, scientists can improve the accuracy and dependability of characterizing rock mass discontinuities from 3D models.

Radiance fields is a new technique to overcome the obstacles in novel view synthesis and inverse rendering, where the intention is to simply create very realistic 3D scenes from 2D photographs. It enables the observation of an object or scene from any chosen position. The radiance field is also capable of simulating view dependent features like highlights and reflections which changes depending on the viewer’s standpoint producing a more realistic rendering.

The Neural Radiance field (Nerfs) and the 3D gaussian splatting (3DGS) are the most popular radiance field approaches currently used, and both are excellent at capturing intricate geometry and illumination (Tosi et al.,

2024).The method uses a deep neural network to generate a volumetric representation of a scene. This network utilizes a 5D coordinates as input, which is made up of the spatial location (x y z) and viewing directions (θ, φ) to produce an output of the volume density and radiance of the scene at that location. The model combines images from various angles to develop new viewpoints that capture the fine visual details and dynamic lighting interactions.

Each point in the scene's colour and volume density are captured by the radiance field, which is defined by the following equation from every possible viewing direction:

$$F(X, d) \rightarrow (c, \sigma) \quad \text{(i)}$$

where:

$x \in \mathbb{R}^3$ is a 3D point in space,

$d \in \mathbb{R}^3$ is a viewing direction (a unit vector),

$c \in \mathbb{R}^3$ is the emitted color (RGB) at that point in that direction,

$\sigma \in \mathbb{R}^3$ is the volume density, which represents how much the points absorbs light (opacity)

The NeRF model for instead uses a neural network representation in which X is the 3D coordinate of the images, d is the azimuthal and polar viewing angles, c is the colour, and σ is the scene's volume density. While the colour c can change depending on both the viewing direction and position, the prediction of σ is made to be independent of the viewing direction in order to maintain multi-view consistency. A Multi-Layer Perceptron (MLP) is used in two stages to accomplish this. The MLP receives X as input in the first stage and produces a high-dimensional feature vector and σ. The colour representation c is then created by combining the feature vector with the viewing direction d and running it through one more MLP (Remondino et al., 2023).

Standard 2D images in many radiance field methods are initially processed through a Structure from Motion (SfM) algorithm just like in photogrammetry. The radiance field model is then trained using the sparse 3D point clouds generated after the SfM algorithm aligns the images. Although, fundamental principle of radiance field methods is the same, the differences in the training procedures due to method used makes the difference between the types of radiance fields.

Unlike the normal meshes, which describe 3D scenes as discrete surface geometries, radiance fields depict 3D scenes as continuous volumetric functions and encode colour and density at every location in space. This allows for the capturing of fine-grained details, complex lighting effects, and transparency that can be modelled with a polygon-based model. Radiance fields are also more adaptable for displaying intricate, photorealistic scenes with view-dependent effects than mesh models which rely on precise topology and texture mapping. Another comparative advantage of radiance fields is the

ability to generate high quality reconstructions quickly with fewer input photos.

2.8 Neural radiance fields (NeRF)

The neural radiance fields (NeRf) technique is based on continuous scene representations using volumetric ray-marching to optimize a Multi-Layer Perceptron (MLP) for novel-view synthesis of the captured scenes. NeRFs use volumetric rendering results with neural implicit representation to provide a continuous scene representation. The scene's geometry and radiance fields are simulated with MLPs, this enables NeRFs to achieve a smooth, high quality scene reconstruction from a sequence of posed images by using the volumetric rendering equation and natural continuity.

The process involves inputting several continuous 5D coordinates, including spatial locations (x, y, z) and viewing directions (θ, ϕ) into the neural network. The algorithm then outputs the volume density (σ) and view-dependent emission radiance (RGB) in each direction at each position (Remondino et al., 2023). After rendering the NeRF from the viewpoints, 3D geometry can be obtained, for example, by marching camera rays to create a mesh.

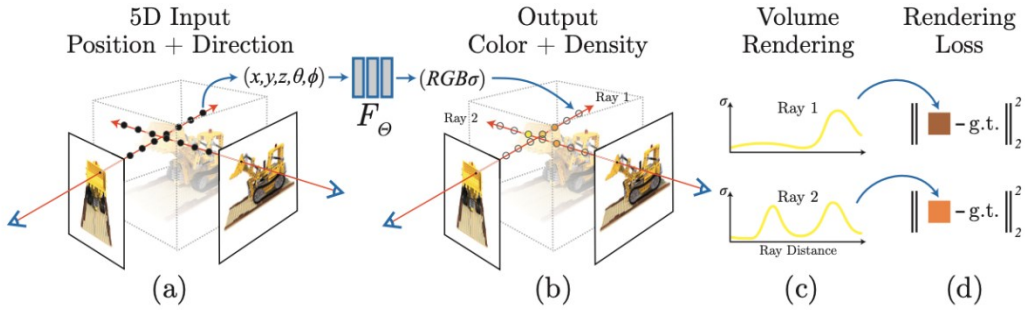

Figure 2. The neural radiance pipeline. Source: (Mildenhall et al., 2020)

Similar to triangle mesh-based techniques, point-based representation can take advantage of the current GPU's effective rasterization process to render in real time. Even though these techniques provide fast rendering speeds and are ideal for editing tasks, they often have gaps and outliers that cause artifacts in the displayed images. This is mainly because point clouds are basic discrete elements, which can leave some kind of gaps in the rendered image.

Neural radiance fields (NeRFs) use a density field and a color field, respectively, to represent the geometry and appearance of a 3D environment in order to automatically produce realistic 3D content. Although NeRFs significantly enhance the quality of the outputs of novel view synthesis, it still has issues with slow training and rendering speeds. The prospective application

of rendering techniques especially for latency-sensitive applications (programs that, in order to operate properly, need a certain amount of time between input and system response) like virtual reality and autonomous driving. For such applications to be useful, speed and effectiveness are an absolute necessity. Therefore a lot of work has been done by researchers to speed up NeRFs so that they can be used on everyday devices like laptops and cellphones, but it is still difficult to find a reliable technique that can render a 3D scene at an interactive frame rate (roughly 30 FPS) on a common device and train a NeRF fast enough (less than 1 hour) on a consumer-level GPU (Wu et al., 2024).

2.9 3D Gaussian splatting

3D Gaussian Splatting is another Radiance Field reconstruction technique that uses an explicit rasterization-based representation instead of an implicit like the Neural Radiance Fields (NeRFs). It is capable of enabling real-time rendering speeds and performance, even on mobile devices, while preserving the outstanding visual fidelity and view-dependent effects for which Radiance Fields are known for. This technique seems to solve the speed problem of NeRFs, it simply uses millions of learnable 3D Gaussians in space to model a scene. It avoids the computational overhead of NeRF-based methods (e.g., computationally expensive ray-marching, and unnecessary calculations in empty space) while maintaining the strong fitting capability of continuous volumetric radiance fields, which is crucial for high-quality image synthesis, by representing scenes with learnable 3D Gaussians (G. Chen & Wang, 2025). 3DGS uses an explicit representation and highly parallelized processes, which enable more efficient calculation and rendering than the implicit, coordinate-based models NeRFs use. This distinctive combination of the advantages of point-based rendering methods with differentiable pipelines is what makes 3DGS innovative.

A Gaussian is basically a smooth, bell-shaped curve that can be adjusted in width, height, and orientation. It is a generalization of 1D Gaussians to 3D space is known as a 3D Gaussian. They have a center, a scale, a rotation, and softened edges, making them ellipsoids in three dimensions.

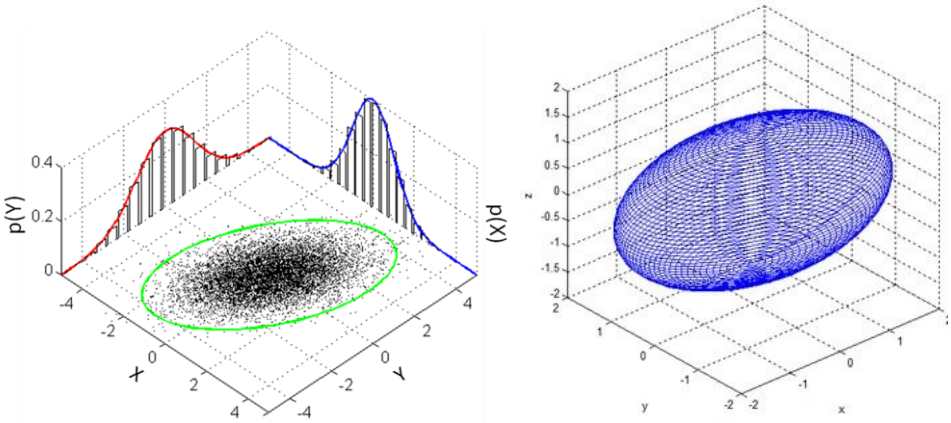

Figure 3. Images of gaussian distribution graphs in 2D and 3D (Bscan, 2013)

3D Gaussian Splatting uses several of these 3D anisotropic balls called splats, each of which is described using a 3D Gaussian distribution to model view-dependent color, and each anisotropic ball has specific characteristics (Fei et al., 2024).

This presents a versatile approach to how a scene can be modelled based on the density and appearance at different positions. With characteristics including position, size, orientation, and color, each 3D Gaussian model represents a volumetric "splat" in a scene. The positions and characteristics of the 3D Gaussians are projected onto the 2D image plane of the camera perspective to create a new scene view (Kerbl et al., 2023). Based on their characteristics and distances from the camera, the 3D Gaussians are converted into 2D "splats" on the image, with all their contributions combined. This is the utilization of Structure from motion (SfM) to start aligning the images for rendering; however Gaussian Splatting produces a sparse point cloud.

The rendering algorithm also ensures that only the visible element of each Gaussian contributes to the final image by considering its visibility and orientation, this ensures a fast convergence (in roughly 30 minutes) and real-time rendering (at least 30 frames per second) at 1080p resolution (Wu et al., 2024). To render surfaces and edges precisely, this involves managing occlusions and utilizing anisotropic (directionally changing) characteristics (Kerbl et al., 2023). Additionally, to cover an entire image, scenes are filled out producing additional Gaussians from the point clouds by a process of cloning and splitting (Cheng et al., 2024). This allows the technique to generate quality visualizations without using a lot of GPU power.

Adaptive density control

3DGS uses an adaptive density control technique to modify the number of Gaussians in order to improve their fit to the scene. In regions that are poorly reconstructed, 3DGS will occasionally generate Gaussians; this process is

known as "densification." At the same time, low-opacity Gaussians will be pruned.

In simple terms, pruning is the process of eliminating unnecessary Gaussians to preserve an effective representation and reduce memory footprint, whereas point densification concentrates on increasing the density of Gaussians in regions that need greater detail, when a scene's training views are extremely sparse, it is difficult to produce high-quality point clouds, which will make scene optimization more difficult. To combat this,(Chan et al., 2024)suggest using the Point Cloud Densification (PCD) technique to create superior point clouds that are denser than the point clouds from the SfM outputs.

The density control procedure concentrates on places where Gaussians are too dispersed or when geometric features are absent. With an emphasis on Gaussians with large view-space positional gradients (i.e., above a given threshold), the densification process will be carried out at regular intervals i.e. after a specific number of training repetitions. It entails splitting large Gaussians in over reconstructed regions or cloning small Gaussians in under reconstructed areas. A duplicate of the Gaussian is made and shifted in the direction of the positional gradient for cloning. When splitting, two smaller Gaussian models are used in place of a larger one, lowering their size by a certain amount. In order to improve the reconstruction's overall quality, this stage looks for the best Gaussian distribution and representation in three dimensions (G. Chen & Wang, 2025).

In the point pruning stage, unnecessary or less significant Gaussians are eliminated; this can be thought of as a regularization procedure. It is implemented by removing Gaussians that are too huge in world-space or view-space, and those that are nearly transparent (with α below a given threshold). The procedure guarantees that the Gaussians in the model continue to be accurate and useful for representing the scene, in addition to helping to conserve computer resources (G. Chen & Wang, 2025)

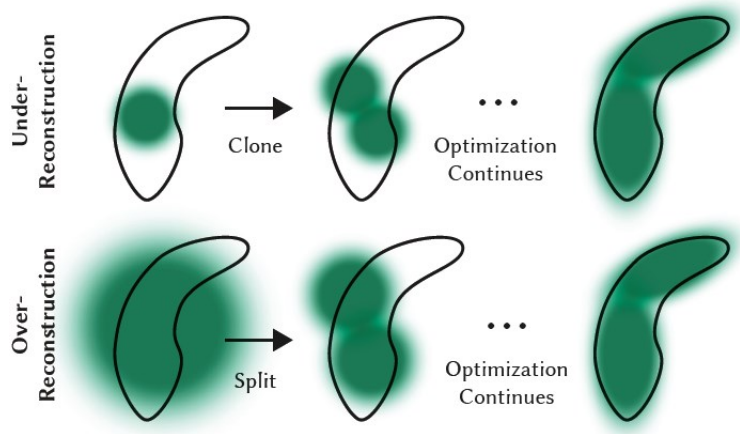

Figure 4. Adaptation of gaussian splats to fit shapes and scenes. Source: (Kerbl et al., 2023)

View dependence

In the real world, a point's colour changes depending on the substance and lighting conditions at different angles. This is best simulated by NeRF and 3DGS using spherical harmonics and view-dependent MLPs (Meng et al., 2024).

View-dependence is the process by which Gaussian Splatting modifies the colours of our 3D object according to the angle of the viewer, giving them a more realistic appearance. To accomplish this, we employ spherical harmonics, which are akin to specialized mathematical instruments that depict colour changes across a sphere.

The concept of view dependence aims to depict how the lighting surrounding an object or in a scene varies based on the viewing angle. By enabling the model to depict non-Lambertian phenomena, such as the speculative nature of metallic surfaces, it gives the depiction a more realistic touch.

The collection of mathematical functions known as "spherical harmonics" can be used to describe patterns on a sphere. Any function on a sphere can be represented by a combination of spherical harmonics, which dictates how colour should change depending on the direction of view. Instead of giving a point (or a "Gaussian" blob in 3D) a fixed RGB colour, the algorithm learns a set of SH coefficients that specify how the colour changes depending on the viewer's angle. Based on your current view direction and the SH formula, it determines the colour when you render that point from a specific angle.

A practical value can be obtained by evaluating such a function for any point on the sphere. The functions are all generated from this one formula by selecting one (ℓ, m) pair per SH and positive integers for ℓ and $-\ell \leq m < \ell$:

$$Y_l^m(\theta,\phi) = \frac{(-1)^l}{2^l l!}\sqrt{\frac{(2l+1)(l+m)!}{4\pi(l-m)!}}e^{im\phi}(\sin\theta)^{-m}\frac{d^{l-m}}{d(cos\theta)^{l-m}}(\sin\theta)^{2l} \quad \text{(ii)}$$

where:

l is the degree (non-negative integer: 0,1,2...),

m is the order (integer: $-l \leq m \leq l$),

θ is the polar angle (from the z- axis),

ϕ is the azimuthal angle (around the z-axis).

The equation becomes significantly simpler for small values of l, for ℓ = 1, Y = ~0.282, which is a constant on the entire sphere. Higher values of ℓ, on the other hand, result in more complicated surfaces. It is possible to express

any function defined on a sphere using SH as the theory states that spherical harmonics constitute an orthonormal

One key view dependence problem however is the fact that 3DGS's has the tendency to interpret some scenes like mirror reflections as distinct scenes and create Gaussian points for them as though they were real, these virtual images inside mirrors are not accurately captured during reconstruction and rendering, which detracts from the scene's authenticity and visual coherence. This was tackled in (Meng et al., 2024)'s study, where a new rendering framework called Mirrow-3DGS was designed to tackle the problem of realistically capturing and drawing real reflections in scenes using mirrors.

2.10 Challenges and limitations of 3d gaussian splatting

The main consideration points for exploring 3D Gaussian splatting as a prospective method of characterizing rock mass is its ability to produce quality visuals from the SfM inputs and the speed of rendering.

Although 3DGS's rasterization-based pipeline provides remarkable real-time performance, it still has drawbacks. The algorithm does not effectively handle highly distorted camera images, which are essential for robotics, secondary rays, which are used for optical effects like reflections and shadows, and stochastic ray sampling, which is required in many other pipelines (G. Chen & Wang, 2025). Low quality rendering in unseen areas is one of the basic rendering issues in this method, if a certain side of an item was not observed by the camera, it may be poorly recreated. These are denoted with Floaters, which are sporadic little artifacts (blobs) that show up close to the camera plane, particularly in regions with sparse data.

Furthermore, in practice, the presumptions that Gaussians do not overlap and can be successfully sorted using only centres are frequently incorrect, resulting in temporal distortions when sorting order is altered by camera movement (Chen & Wang, 2025). Some Gaussians may grow overly large, overextended, redundant, or even ineffective during training. Therefore, in order to maintain stability, manual fixes, also known as regularization heuristics, are often added to remedy that.

The appearance of artifacts in regions with inadequate observational data is a significant problem with 3DGS. This problem is a common restriction in radiance field rendering, where reconstruction errors are frequently caused by sparse data. Reconstructing scenes from restricted views is of great interest from a practical standpoint, especially because it can improve functionality with little input. In comparison, NeRFs, on one hand, employ neural network MLPs, which function similarly to smooth paintbrushes; they seamlessly blend objects by "filling in the gaps" between recognized views.

Conversely, Gaussian Splatting does not exhibit this smoothing behaviour and instead employs discrete points (Gaussians). Therefore, it may not look good if the visualizations are not taken from enough angles because the method is less "forgiving" and more sensitive than NeRF.

The modelling of priors is the main problem of 3DGS for sparse inputs because it uses either feed-forward Gaussian models, generative models, or depth information and this results in a primary trade-off between generalizing with learnt priors or overfitting to the views that are now available (G. Chen & Wang, 2025).

The integration of machine learning and its use in radiance fields is leading a transformative shift in the way photogrammetry for rock characterization has been done in the past, with the subsequent release of 3D Gaussian Splatting (3DGS) as a 3D rendering technique that offers a more flexible, efficient, and accurate representation of geometry and appearance, all by modelling surfaces as collections of Gaussians (Fei et al., 2024). This method not only enhances rendering speed and visual realism but also provides unprecedented control over scene dynamics, currently making it a powerful tool in computer vision and graphics.

The adeptness of 3DGS to is to enable real-time, high-resolution rendering without significant computational overhead. From virtual and augmented reality to cinematic rendering and real-time simulations, this technology has been unlocking all the possibilities previously constrained by hardware limitations. Moreover, as a radiance field method, its explicit scene representation and efficient rendering pipeline makes it a superior technique for handling complex geometries and dynamic lighting conditions (G. Chen & Wang, 2025).

As research continues to refine and expand the capabilities of 3D Gaussian Splatting, its role in scientific visualization, environmental modelling, its applicability in rock mechanics. By overcoming the limitations of traditional rendering paradigms, 3DGS is poised to redefine the future of 3D scene representation and establish itself as a cornerstone of modern computational graphics.

3 RESEARCH MATERIAL AND METHODS

3.1 Description of test site

The data for the thesis was taken from the Underground Research Laboratory of Aalto University (URLA). Aalto University's Underground Research Laboratory (URLA) is situated under the Otaniemi campus in Espoo, Finland. It is a 20-meter-deep system of interconnected tunnels in granitic rock that is used for research. The data was specifically gathered in tunnel 11, around 20 meters from the entrance from the Engineering School.

The defined boundary space in that section of the tunnel walls, the lighting configuration, and the unique characteristics of those walls (the tunnel water flow through the walls, the many discontinuities, and the absence of shotcrete cover and reinforcements) led to the selection of this location. Although migmatic granite and hornblende-biotite are the predominant rock type in this tunnel according to literature (Janiszewski et al., 2022), the lithological map from the Geological Survey of Finland shows the area to be predominantly made of granodiorite instead.

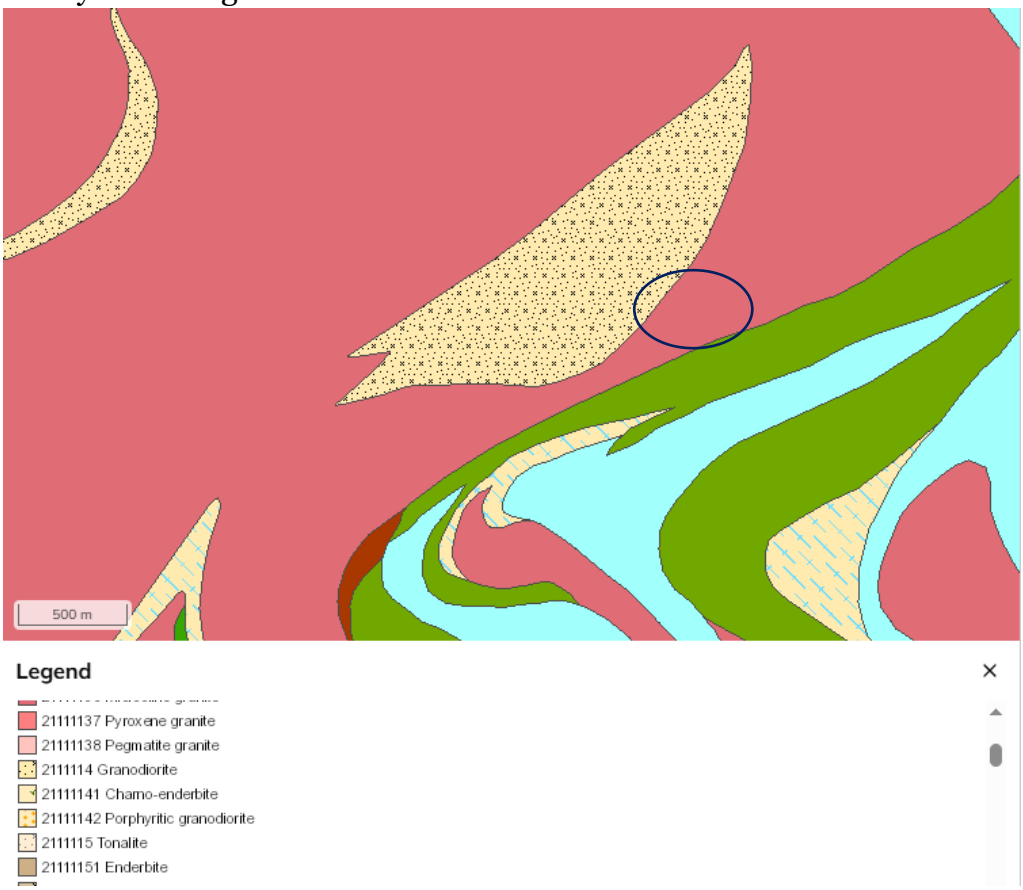

Figure 5. Lithographic map of test area from Geological Survey of Finland (GTK)

3.2 Data acquisition procedure

The primary data collecting methods for determining the point clouds and the separations between points in the tunnel were motion photogrammetry, smartphone videogrammetry, and laser distance meters.

3.3 Hardware selection

- Canon EOS-1DX Mark II DSLR camera
- Tripod
- Remote capture device
- Orientation control boxes
- Dewalt LED work lights
- Leica Disto S910 laser meter

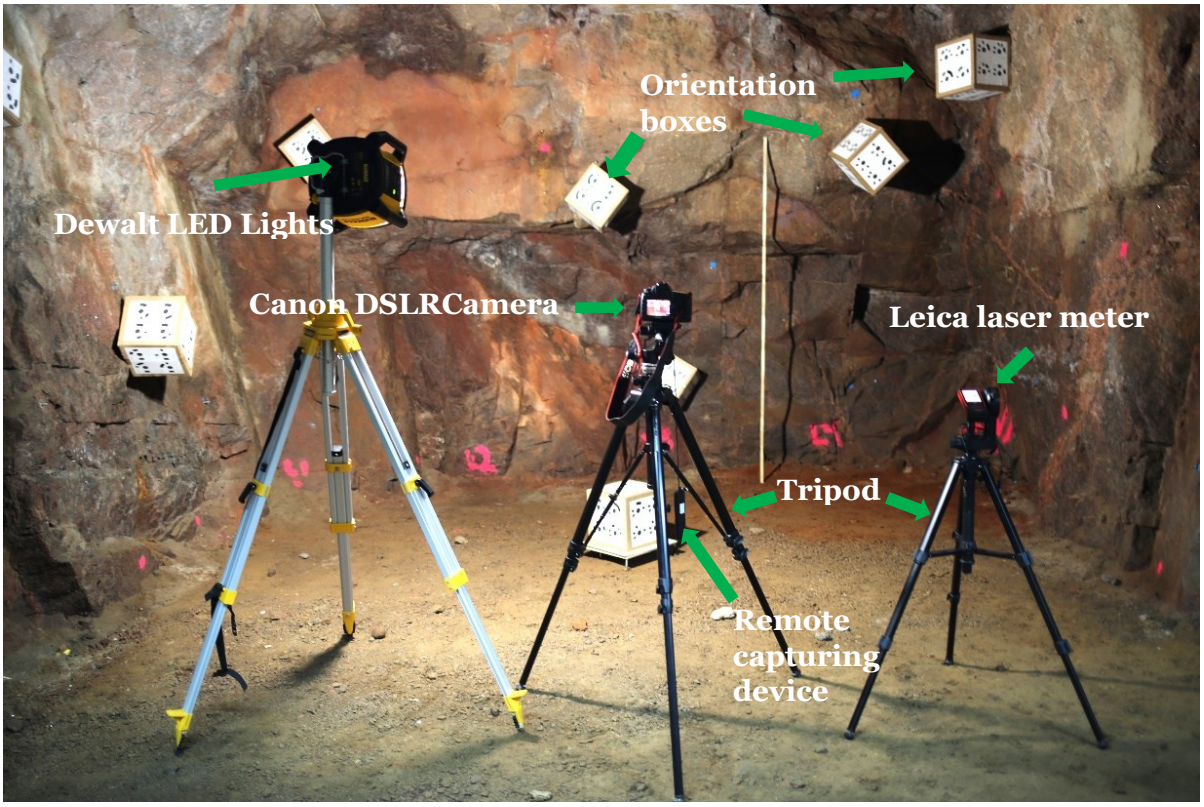

Figure 6. The primary setup of the equipment in the tunnel working area

- The smartphone device used was a Samsung Galaxy A14 with Android version 14, storage capacity 64GB, 6.6 inch diagonal LCD Multi touch display, 1080 by 2408 pixel resolution.

- The personal computer had the following specifications: Windows 10 pro, Intel(R) Core(TM) i9-9900K CPU @ 3.60GHz 3.60 GHz, 64.0 GB RAM, Nvidia RTX 2080 Ti GPU

3.4 Image acquisition

Photos were taken in the tunnel for the structure from motion with the DSLR camera. Using a tripod, the images were taken at three different elevations: roughly one meter above the ground, two meters above the ground, and three meters above the ground. The 2m elevation was taken straight, without any angling, capturing all three sides of the tunnel walls. The 1m elevation was oriented such that the camera was gazing above, while the 3m elevation inclined the camera downwards.

The 3D model was scaled and oriented using seven alignment boxes, four of which were on the rock surface and one on the ground. A geological compass was used to point the alignment boxes on the ground in the direction of the north.

3.5 Camera settings and photo editing

For the setup to yield high-quality photos, the camera settings were adjustment to the specific scene conditions. Due to the external lighting provided in the tunnel, a low ISO sensitivity setting was chosen to reduce the grain or digital noise, and a small aperture was chosen to regulate the amount of light entering the lens and to enhance depth of field, which sharply focused the background and foreground. To achieve the maximum amount of overlap in the photos for the motion processing framework, an ultra-wide-angle lens was utilized to obtain a broad field of view each image.

Table 1. captures the relevant camera settings used in the data collection

Parameters	Value
ISO speed	200
Focal length	14mm
F-stop	f/11

Figure 7. The Canon EOS-1DX Mark II DSLR with the camera settings used in the data collection

3.6 Control points and control distances

Orientation control boxes were used to scale the and rotate the 3D model accurately. Each box consisted of five visible faces with four control points per face, positioned at distances from each other. The primary control box was mounted on a flat horizontally levelled board placed in the scanned scene and aligned using a geological compass to ensure that all the points lie on a horizontal plane and the arrow pointed to the north direction. The distance from the top of the box to the ground surface was averagely 33 cm.

In addition to the main box, 7 supplementary boxes were positioned along the tunnel surface to assess and compare model's geometric accuracy. Each control point consisted of a 20-bit circular single ring marker, with four markers affixed to each face of the box.

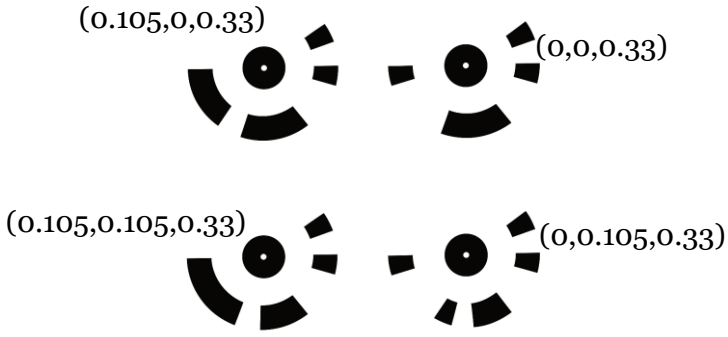

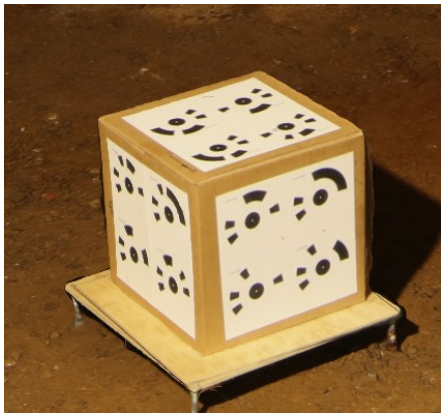

Figure 8. Orientation control box with known distances between control points and the orientation control box used in the test.

3.7 3D models from the point clouds

A dense point cloud of the scene was generated with the RealityCapture 1.5.1 from epic Games. However, during the time period of the project, Reality Capture was renamed as RealityScan 2.0.1 in their next software update but the majority of this project was completed on the RealityCapture 1.5.1. With the photogrammetric method, the tunnel surfaces in the 3D models were meshed from the point clouds after they were aligned in the same software. However, with the Gaussian splatting approach, the aligned point clouds are imported into the Gaussian splatting software used – Postshot, Blender, SuperSplat. All the point clouds are left to be tie points except the four markers shown in Figure 8, which are converted into ground control points for the alignment of the model.

Prior to computing the model, certain pre-step setup had been done, such as setting the ground plane and readjusting the reconstruction region to include the scene's overall size in the proper direction.

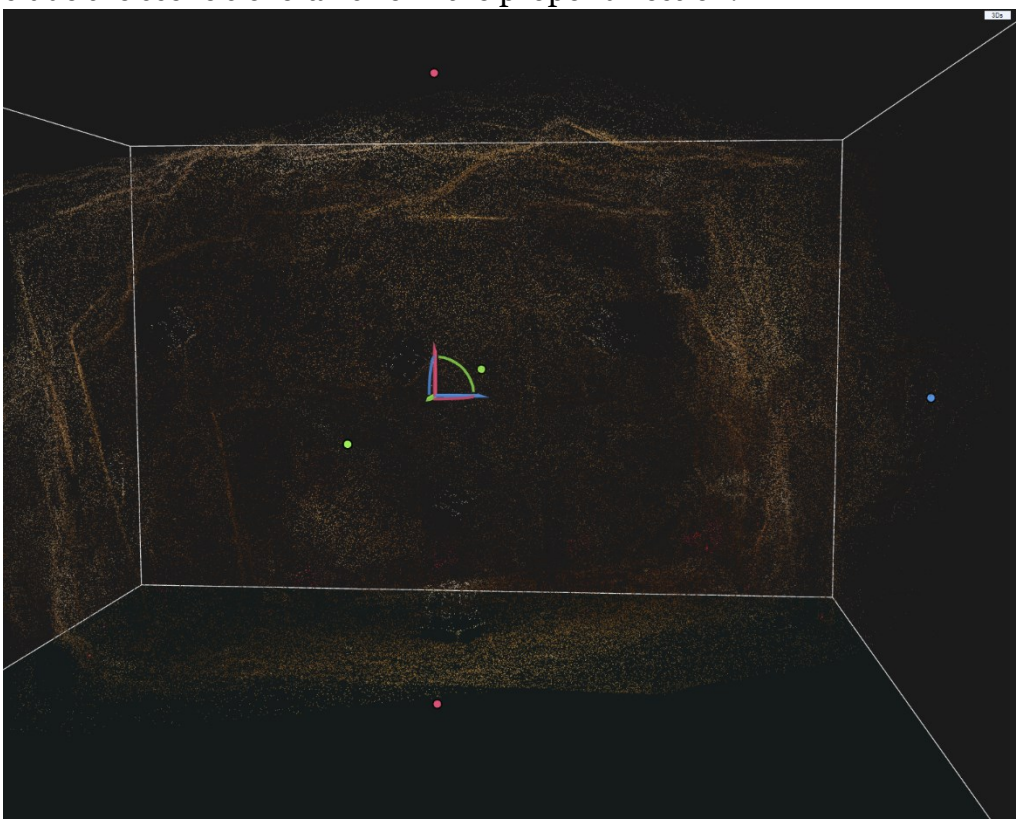

Figure 9. Unaligned point cloud of model from Reality Capture

3.8 Gaussian splatting software

Three different software algorithms were used to visualize the 3D gaussian splats to check the visual quality of the splats as the method develops. The same input data visualized in the different software produced quite different visual output.

Jawset Postshot

Jawset Postshot is a software for creating photorealistic 3D scenes and objects using Radiance Fields technology. The main advantages of postshot for Gaussian splatting processing is the ability to allow local processing, loading and exporting of PLY files, ease of edits, and the interactive previews during training. Among all the gaussian splatting applications used, Postshot produced the best visual quality; unfortunately, the current versions of the program lack any measuring capabilities. As a result, the distances acquired from Postshot were measured using 3D Vista as a post-processing step.

Figure 10. The postshot window displaying the rendering settings and the processed splats

SuperSplat

Supersplat (PlayCanvas, 2025) is an open-source, browser-based software for editing and optimizing 3D Gaussian Splats. It is built on the PCUI front-end framework and PlayCanvas Engine runtime. The main features that made it a suitable option for this thesis are the ability to load PLY files, delete individual splats and crop sections of interest in the scene. The scenes created using SuperSplats had a respectable level of visual quality, with objects' features visible up to a very high magnification point. The software provides a lot of parameters for the training of the gaussian splats, however, the lack of an integrated measurement capability in the user interface made this software unsuitable for the measurement part of this research, therefore, it was only utilized for the viewing of the models, no measurements were made using it.

Figure 11. The 3DGS model as visualized in SuperSplat

Blender Version 4.4.1

In this research, the exported 3D gaussian model was visualized using Blender, a free and open-source 3D computer graphics application.
Although Blender cannot handle 3DGS on its own, the Kiri engine 3DGS Addon V2 for Blender can expand Blender's capabilities to edit and render 3DGS. Only Blender 4.2 and later versions were compatible with the extension. Since the Blender software was not initially designed to handle the spheric harmonics displayed in the Gaussian models, it was crucial to continuously update the camera view in order for the software to render the Gaussian splat model using the point clouds as PLY files from the Reality Capture software.


Figure 12. The 3DGS model as visualized in Blender

Scaniverse

Niantic's Scaniverse (Niantic Spatial, 2021) was the smartphone application utilized in this research. Real-time, high-quality models of objects, spaces, and scenes were captured with it. The mobile device is where all the processing and output takes place. It requires a slow, natural speed movement to wander around the backdrop or object of interest, and it took around one to five minutes to capture an entire scene. Using the same concepts as videogrammetry, it is necessary to record high, medium, and low elevations both close and far away.

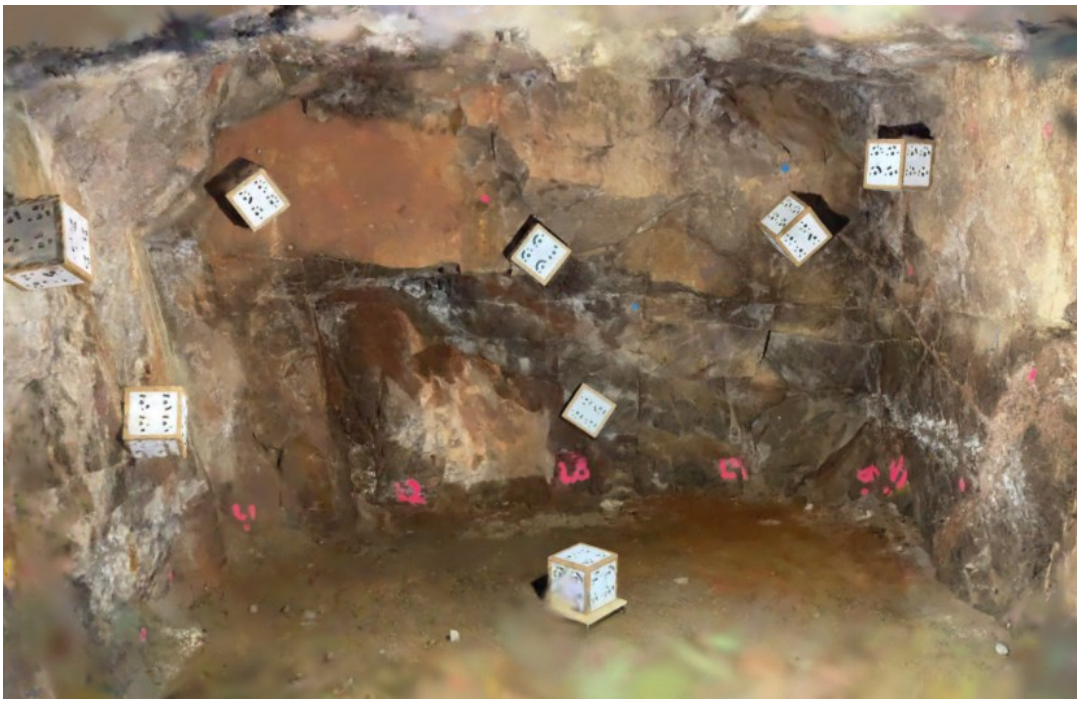

Figure 13. A screenshot of the scaniverse model of the test site, processed and modelled by a smartphone

3.9 Photogrammetric processing workflow

Processing the photogrammetric model in Reality Capture followed the following roadmap.

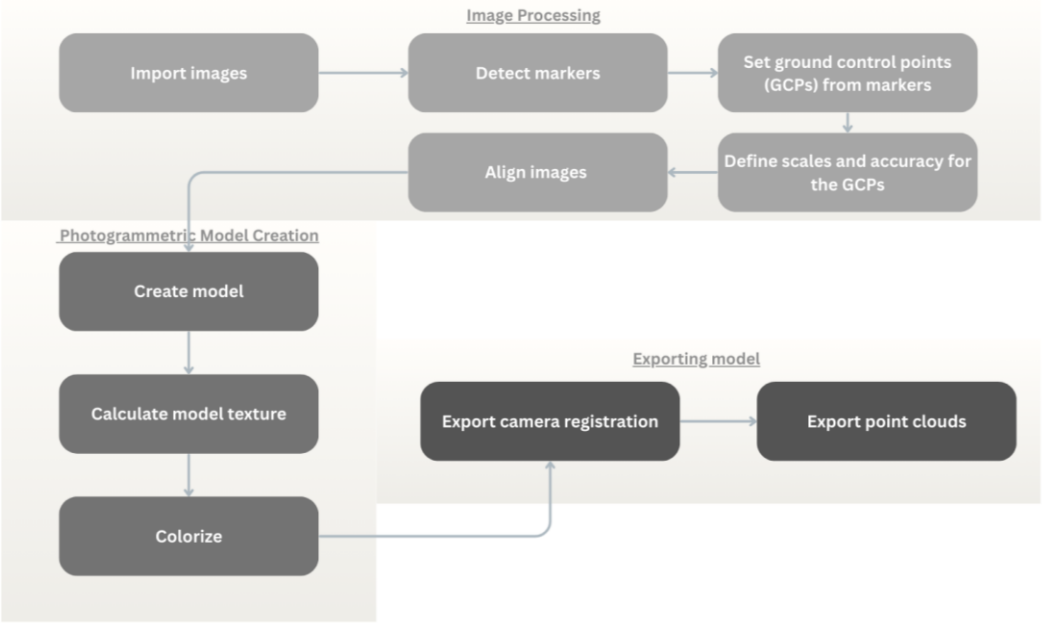

Figure 14. The workflow of the Reality Capture model

All photographs captured with the DSLR camera were first separated into two datasets: the RAW files (CR2 format) and the compressed JPG files. The JPG images were imported into RealityCapture using the Add Imagery function within the Workflow tab, as these provide faster processing while retaining sufficient detail for photogrammetric reconstruction.

Under the Alignment tab, the software automatically detected all 20-bit circular single-ring coded markers present in the imagery using the Detect Markers tool. Four of these markers—positioned on the ground above the orientation control box—were assigned as ground control points (GCPs). Their coordinates were manually entered to match physically measured distances, ensuring that the resulting model adhered to a correct spatial reference and scale.

The images were then aligned to compute camera poses, image features, and a sparse point cloud. After achieving a successful alignment with acceptable residual errors, a dense point cloud and a polygon mesh were generated at Normal Detail to produce a high-quality geometric reconstruction of the tunnel face.

RealityCapture's texturing module was subsequently used to colorize the mesh, generating a detailed and accurate RGB surface representation suitable for visualization and further analysis.

To ensure compatibility with the Gaussian Splatting workflow, both the internal and external camera parameters were exported in .csv format and saved in the same directory as the JPEG images. The colored dense point cloud was also exported in .ply format and placed in the same folder. These exported files—.ply point clouds, .csv camera parameters, and the original images—served as the required inputs for subsequent processing in Jawset Postshot.

3.10 Gaussian splatting processing workflow

The Postshot Gaussian splatting model also followed the roadmap as laid out by Balabanian, (2024).

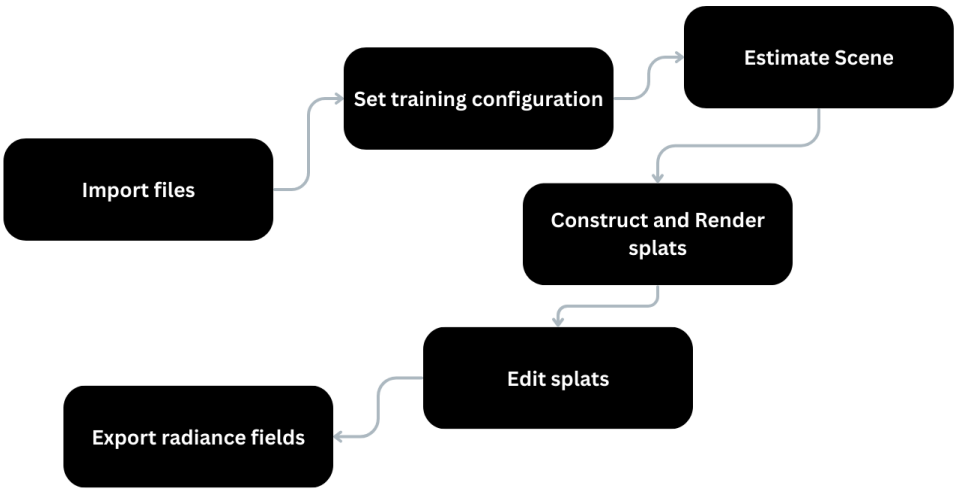

Figure 15. The process in processing the gaussian splats in Postshot

To generate the 3D Gaussian Splatting model, the processed outputs from RealityCapture were first prepared for import into Jawset Postshot BETA. The point cloud file exported from RealityCapture (.ply) and the corresponding camera parameter file (.csv), together with the original JPEG images, were placed in the same working directory to ensure proper scene initialization. A total of 129 tunnel images were used in this workflow.

All assets—the images, the .csv camera poses, and the .ply point cloud—were imported into Jawset Postshot. The Image Selection setting was configured to use all available images, as the dataset size (≈100–130 images) was suitable for complete multi-view coverage while ensuring stable camera alignment. Camera poses were directly loaded from the RealityCapture .csv file, ensuring consistency in camera intrinsics/extrinsic between the photogrammetric and 3DGS reconstructions.

The training configuration was set as follows:

- Radiance Field Profile:

Splat3 (Radiance Field) was selected because it provides the best reconstruction performance for high-resolution DSLR imagery. This profile is optimized for preserving fine-scale textures and contrast transitions, allowing both background and foreground details to be accurately represented in the splat radiance field.

- Maximum Splat Count:

The upper limit was set to 3000 splats. This constraint was chosen to maintain a balance between visual detail and computational efficiency, reducing GPU memory and storage requirements while retaining the necessary geometric structure for engineering measurements.

- Image Downsampling:

All images were downsampled to 3840 px width to reduce training overhead while preserving sufficient resolution for high-quality splat rendering.

- Training Duration:

Training was configured to stop at 30,000 steps, since most of the model convergence occurs early in the optimization process. Beyond this threshold, improvements in visual fidelity are marginal while computation time increases significantly.

Once training commenced, the Jawset Postshot software automatically initialized the scene using either a multi-view stereo (MVS) or structure-from-motion (SfM) procedure (depending on internal heuristics), from which the radiance field and early splat primitives were generated.

After training, the model was refined using the Crop Box tool within the Radiance Field tab to isolate the relevant region of the tunnel face. Unwanted artifacts—primarily "floaters" or incorrectly placed splats—were manually removed using the selection tool to ensure a clean and metrically reliable model.

Finally, the completed radiance field was exported in .ply format for further measurements and analysis.

3.11 Evaluation of device-based differences in gaussian splatting visualization

The differences in measurement accuracy and visual rendering quality of 3D Gaussian splatting when visualized on a smartphone versus a personal computer (PC) was evaluated.

The software platform used for the visualization is the SUPERSPLAT v2.8.1 because it is a web-based software which can be assessed from any device with a web browser. However, since there are no measurement functions in the Supersplat software, two different software are used for the measurements, Blender for Pc and Scaniverse for the smartphone.

The same pre-processed data with 1M splats was uploaded into the Supersplat software on both devices.

In the computer image, the sharpness, colour, noise and completeness were checked with the Postshot model, and the image showed a fine detail of the reconstructed splats, and it retained the same colour coding as the original splats from Postshot.

Figure 16. The 3D gaussian model as visualised on a computer with Supersplat

The same criteria (sharpness, colour, noise and completeness) were used when comparing the mobile phone model. The phone retained all the features of sharpness, colour, noise and completeness as the computer model. However, due to the screen size and refresh rate of this particular device, the movements within the model were not as smooth as that on the computer.

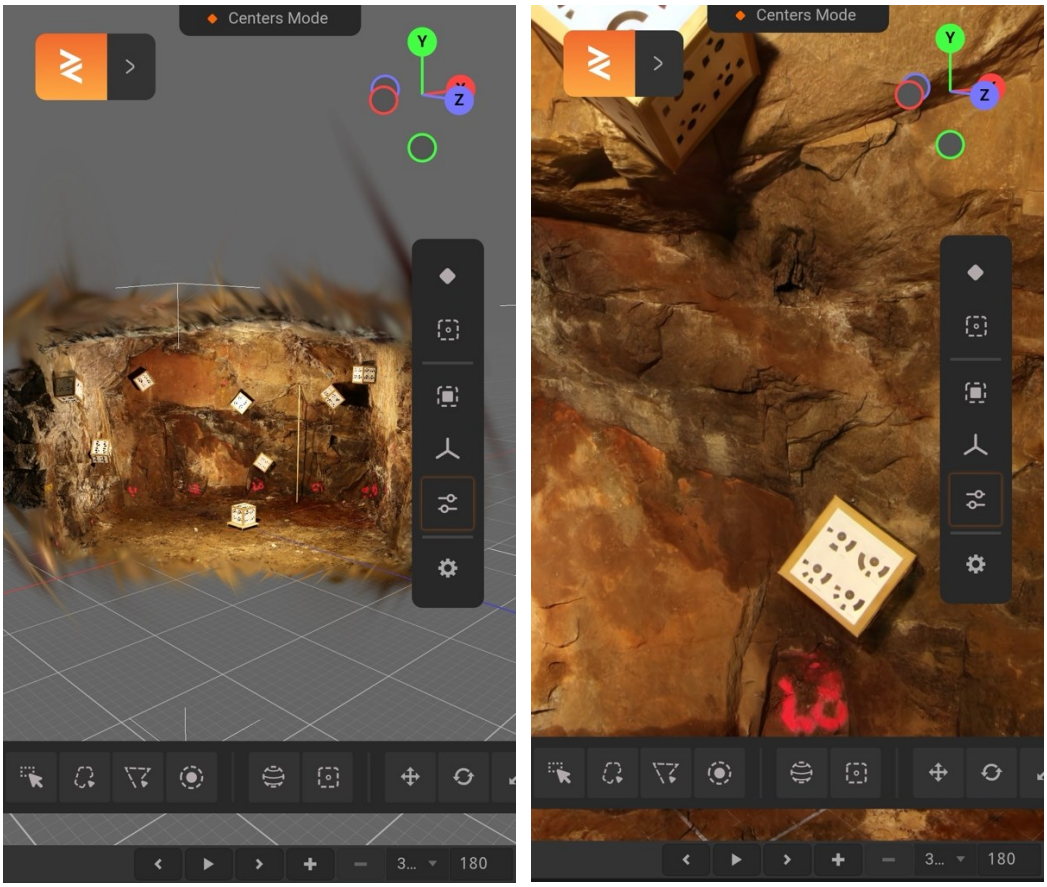

Figure 17. one full scale view of the scene and one close-shot view of the mobile phone model as seen in Supersplat

3.12 Comparing Rock Quality Designation (RQD)

In assessing the accuracy of the 3D gaussian splatting software for rock mass characterization, the method was compared to manual RQD measurements and RQD measurements from a photogrammetric model. A total of 5 scanline measurements were taken on the rock surface across the study area. The scanlines were placed vertically on the rock surface to ensure representative sampling. The scanline positions were marked in the field and measured; a Two (2) metre measuring rule was placed at each scanline position as shown in the picture below.

Figure 18. An image showing the scanline positions for the RQD measurements

3.13 Physical RQD measurement

The RQD is widely used index in the mining and rock engineering discipline to measure rock mass quality. More commonly, this method uses drill cores to detect where discontinuity spacing frequency and where it occurs to determine how it affect will the rock mass. However, in tests where drilling is not easy to achieve like in this experiment, a non-destructive method of using scanlines is implored to measure the RQD of the tunnel.

A physical measurement of the RQD was first done in the tunnel as a control for the rest of the experiment. In this measurement, the equipment used included a measuring rule and notebook for field data recording.

A 2m measuring rule was carefully placed perpendicularly to the major joint planes, which was moving horizontally along the tunnel section, therefore most of the scanlines were placed vertically with its start point from the top and end point on the ground. The discontinuity locations that intersected the measuring ruler were read from the top of the ruler to the bottom and the values recorded for all the 5 scanlines. The continuous segment lengths longer than 10cm were then used to compute the RQD using the formula

$$RQD = \frac{\Sigma\, length\ of\ segments{>}10cm}{Length\ of\ Scanline} \times 100. \qquad \text{(iii)}$$

3.14 Photogrammetric RQD measurements

In computing the virtual RQD measurements, the same 5 scanlines were digitally recreated by aligning the top and end points to match the field coordinates. The discontinuities intersecting the two (2) metre virtual scanlines were visually identified from the normal detail 3D mesh of the model. The segments between discontinuities were measured using the define distance tool in Reality Capture, the virtual RQD was computed with the same formula in (iii) as the physical measurements.

To enhance measurement accuracy and precision for the photogrammetric measurements, a point-cloud-based approach was also adopted using the CloudCompare software, which is an open-source software widely used in geotechnical and engineering geology applications like this. Unlike mesh-based analysis, CloudCompare allowed RQD measurements to be made directly on the raw photogrammetric point cloud, eliminating the geometric interpolation step. This ensured that discontinuity boundaries and surface irregularities are represented with higher fidelity to the original capture geometry.

In this improved workflow, the same photogrammetric datasets used in RealityCapture were exported as dense point clouds and imported into CloudCompare. Scanlines were manually drawn along the rock face, and discontinuity segments were measured following the same procedures applied in the field and other digital methods (e.g., Postshot).

3.15 Cloud Compare RQD measurements

The photogrammetric method used with RealityCapture made the RQD measurements on the textured mesh, however, for very good accuracy and precision in measurements, it is more preferably to use a point cloud-based approach to make the measurements on the point clouds themselves. For this reason, CloudCompare was used as an alternative photogrammetric measurement method. The resulting RQD values were then compared against both physical field measurements and mesh-based measurements from RealityCapture to assess differences in accuracy and correlation. Detailed results of the measured RQD using CloudCompare can be seen in Appendix C

Measurement workflow in CloudCompare

The point clouds and mesh of the model was prepared in Reality capture and exported imported into .ply and .obj respectively.

The point clouds and the mesh were then imported into the CloudCompare software.

The polygon tool was used to mark the locations of the 5 scanlines.

To measure the distances between the discontinuities, the point picking tool was used to pick up the points of interest and the values of each segment of the scanline was documented

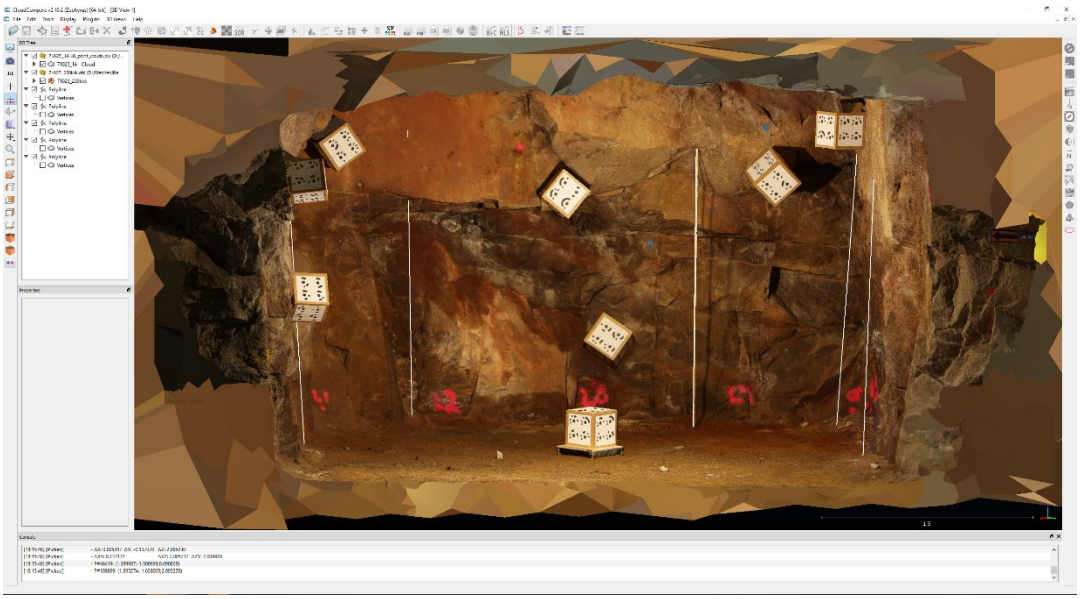

Figure 19. The CloudCompare Window showing the marked scanlines.

4 RESULTS

This section presents the outcomes of the field data acquisition, photogrammetric reconstruction, Gaussian splatting processing, and validation of 3D distance measurements. The goal was to assess the geometric fidelity and measurement accuracy of the Gaussian splatting reconstruction against real-world tunnel measurements.

4.1 Field measurements

To establish ground truth, three sets of known distances were physically measured in the tunnel using a laser rangefinder. Each distance was measured five times to assess precision as seen in the Appendix A. These distances represent a determined short, medium, and long spatial spans in the tunnel as seen in the figure 20 below.

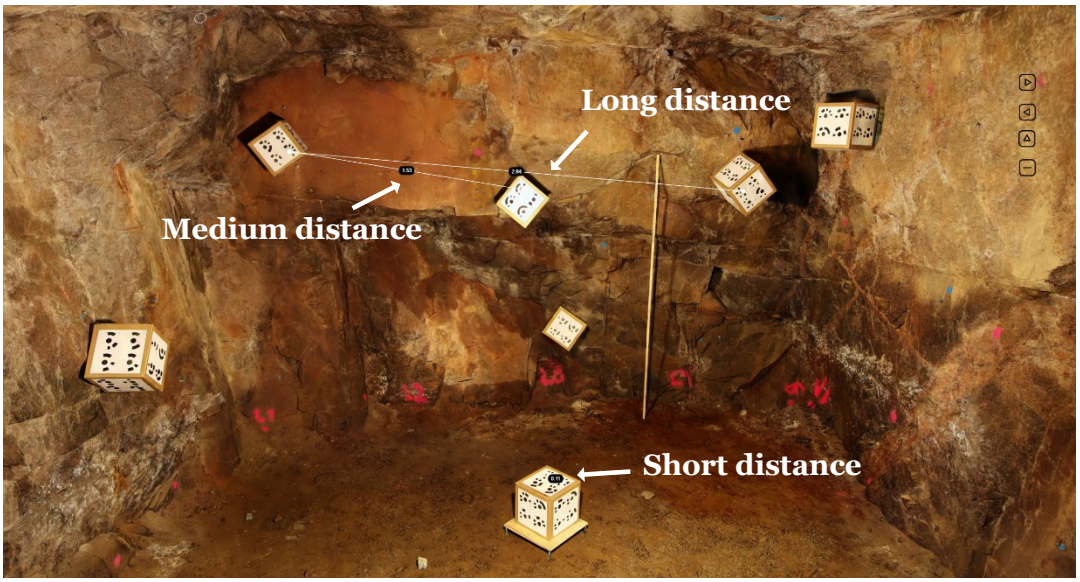

Figure 20. The determined short, medium and long distances measured in the tunnel

Table 2. Physical Distance Measurements (Mean + SD)

Distance Type	Location Description	Mean Distance (m)	Std. Dev. (m)
Short	Between two marker points on the same box	0.1067	0.00089
Medium	Between two marker points on two adjacent boxes	1.5316	0.00203
Long	Between the marker points on the boxes at the corners of the tunnel	2.9482	0.00588

The mean distance of the five measured distance type was used as a representative value for that distance type.
The low standard deviations is a good indication of high measurement consistency between the measured distances.

4.2 Comparison of physical and virtual measurements

Distances were measured within the Gaussian splatting environment (3D Vista Tour Pro) and compared to the physical ground-truth data.

Table 3. Comparison of physical, photogrammetric and Gaussian splat measurements

Distance Type	*Physical (m)*	*3D Gausssian Splating Models(m)*			*Photogrammetric Model*
	mean	Postshot + 3D vista	Blender	Scaniverse	Reality Capture
Short	0.1067	0.104	0.106789	0.11	0.11
Medium	1.5316	1.53	1.51294	1.53	1.53
Long	2.9482	2.94	2.94107	2.95	2.95

The comparison of physical distances with those derived from 3D Gaussian Splatting (Postshot + 3D Vista, Blender, Scaniverse) and photogrammetry (RealityCapture) shows excellent agreement across all distance scales.

For the short distances (~0.1 m), deviations from the physical mean (0.1067 m) were ≤0.007 m, with Blender reporting higher numerical precision (six decimals) while other software rounded to two or three decimals.

For medium distances (~1.5 m), all models were within 0.02 m of the physical mean (1.5316 m), again with Blender showing more significant figures than the other platforms.

For long distances (~2.95 m), deviations were ≤0.01 m across all models, confirming consistent accuracy regardless of scale.

Overall, both Gaussian splatting and photogrammetry reproduced physical measurements with near-equivalent precision. The small differences observed are primarily due to variations in the number of significant figures reported by each software, rather than genuine measurement error.

Table 4: Error Comparison of physical, photogrammetric and Gaussian splat measurements

Error Postshot (m)	**Error Blender** (m)	**Error Scaniverse** (m)	**Error RealityCapture** (m)
-0.0027	8.9E-05	0.0033	0.0033
-0.0016	-0.01866	-0.0016	-0.0016
-0.0082	-0.00713	0.0018	0.0018

The error values for Postshot, Blender, Scaniverse, and RealityCapture relative to the physical baseline shown in Table 3 shows that;

For the short distances, all the methods produced very small errors (<0.005 m). Blender reported the lowest deviation (8.9×10^{-5} m), while Scaniverse and RealityCapture recorded slightly higher but still minimal errors (+0.0033 m).

For medium distances, Postshot, Scaniverse, and RealityCapture showed consistent results (−0.0016 m), while Blender reported a larger deviation (−0.0187 m). This suggests that Blender's higher precision output does not always correspond to improved accuracy.

For long distances, Postshot (−0.0082 m) and Blender (−0.0071 m) slightly underestimated compared to physical measurements, while Scaniverse and RealityCapture slightly overestimated (+0.0018 m).

The magnitude of errors across all software platforms remained very small, generally below ±0.02 m, indicating high reliability of both Gaussian splatting and photogrammetry in reproducing physical distances. The variation between platforms is more related to software-specific processing and reporting differences than to systematic measurement bias.

4.3 Visual quality assessment

The visual quality of the Gaussian-splatted models was evaluated qualitatively based on clarity of discontinuities and feature smoothness.
Side-by-side comparison of Photogrammetric (Reality Capture) mesh and Gaussian splatting (Postshot) output.

- **Reality Capture**: Dense point cloud but aliasing visible on edges.
- **Gaussian Splatting**: Smooth surface representation with high fidelity in crack features and wall textures.

Postshot

Figure 21. The visual quality of the postshot model

Reality Capture

Figure 22. The visual quality of the Reality Capture model

The visual quality of the splats in the Jawset Postshot model shows the scene more brightly lit, more visible in the window due to the contrast created by the darker background behind the model. The rendering enhanced colour differentiation and made textural features more discernible. However, closer inspection revealed a dispersion of splats toward the edges of the model and the presence of floating splats that extend beyond the primary surface boundary. The absence of clear, defined edges can be ascribed to the adaptive density control, which leads to variable shapes and sizes of the splats, this introduces a softer and less geometrically constrained appearance. Although this contributes to a more organic rendering, it slightly reduces structural sharpness compared to mesh-based representation in the Reality Capture model. The postshot model also produced a more complete model, effectively filling in regions where point density was low or image overlap was insufficient. This interpolation capability allowed the scene to appear continuous and visually coherent, even in areas of sparse data.

The RealityCapture model shows a highly detailed surface geometry and detailed textures from the calibrated images. However, while the texturing in RealityCapture is generally crisp and close to the captured material, its overall appearance tends to be lacklustre and incapable of automatically modifying the lights' colour, intensity, and direction in response to movement or shifting perspective (dynamic lighting). The uniform illumination and absence of ambient shading in the RealityCapture rendering result in flatter visual outputs that appear less realistic when compared to the brighter, more visually contrasted Postshot model. Furthermore, RealityCapture did not interpolate or reconstruct areas with insufficient point cloud data, resulting in visible grey patches or untextured gaps in the final model.

4.4 Rock Quality Designation

The rock quality designation results for the 5 scanlines as measured on the field and with Reality Capture. Due to the close similarities in the RQD values, the number of segments generated in each model, the lengths of the segments were also considered in the comparison.

RQD values were computed over five scanlines using the three different methods: the digital measurements from Postshot representing Gaussian splatting models, the photogrammetric digital measurements from RealityCapture, and the traditional physical measurements. The outcomes from each scanline segment are displayed in the Appendix B.

Table 5: shows the comparison of the difference in the RQD measurements between the Physical (Phy), as the reference and the digital methods; Photogrammetric (RealityCapture = RC and CloudCompare = CC) measurements and the 3D Gaussian splatting (Postshot = Po) measurements. AD = Absolute difference.

Scanline	RQD Phy	RQD RC	AD (Phy-RC)	RQD Po	AD(Phy-Po)	RQD CC	AD (Phy-CC)
1	95	96	1	100	5	95.5	0.5
2	91.5	87.5	4	93.5	2	92.5	1
3	100	91	9	95.5	4.5	96	4
4	97.5	100	2.5	97.5	0	100	2.5
5	86	81.5	4.5	87	1	86	0
Mean	94	91.2	4.2	94.7	2.5	94	1.6

Physical Vs Photogrammetry

Figures 24 and 25 illustrate the results in Table 5 with a bar chart showing RQD values for each scanline between the photogrammetric model measurement and the physical measurement, and a scatter plot comparing photogrammetric measurements vs. physical measurements.

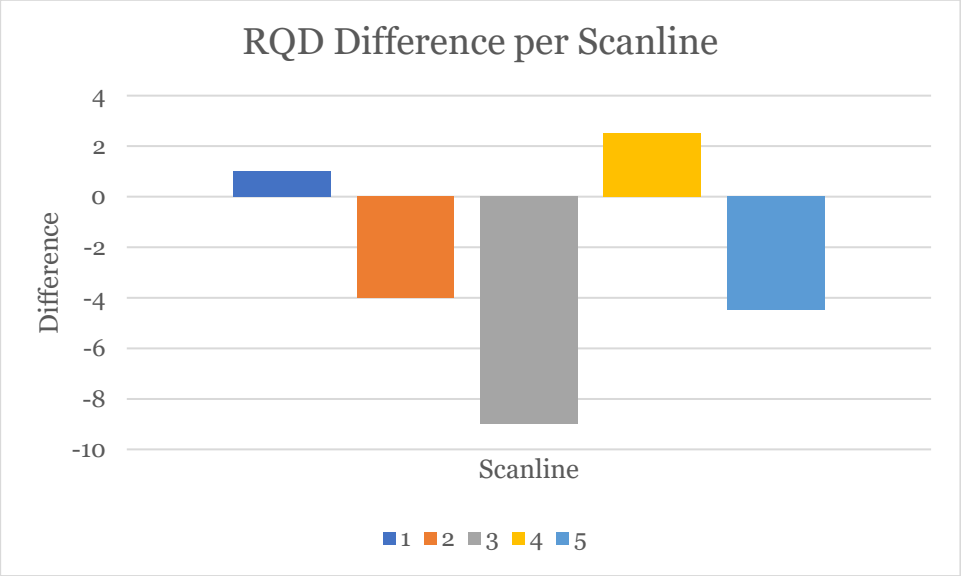

Figure 23: shows the RQD difference between the physical measurements and the photogrammetric model measurements in a bar chart

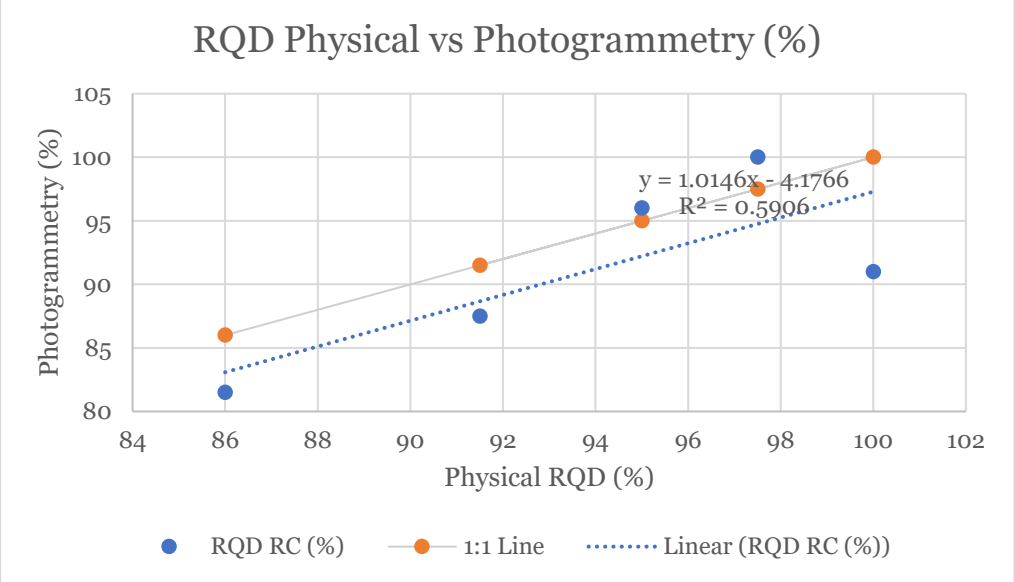

Figure 24: shows the correlation graph of RQD measurements between the photogrammetric model measurements and the physical measurements. The orange dots indicate the 1:1 correlation, if the scanlines were all perfectly correlated, what was supposed to be observed. The blue dots on the other hand indicate the actual correlation points between the manual and 3DGS for every scanline, with the blue dotted lines showing the trendline of the actual correlation. (RC = RealityCapture)

Pearson's correlation coefficient: r = 0.76852

The RQD measurements between the Physical and the Reality capture showed differences in RQD values of as low as 1% in the scanline 1 measurement, up to as high as 9% difference in the scanline 3 measurement, making mean absolute difference of 4.2.

The correlation analysis between the photogrammetric values and the physically measured RQD values revealed a moderate positive relationship, $R^2 \approx 0.59$. The regression line equation suggests the photogrammetric measurements slightly underestimated the RQD at lower values and overestimated it at higher RQD ranges, as indicated by the slope slightly above unity and a small negative intercept.

The results demonstrate that the photogrammetric model effectively reproduces the general trend of the physical RQD measurements. The deviations can be attributed to image alignment errors, lighting inconsistencies and limited visibility of fine discontinuities in the photogrammetric reconstruction.

The moderate-to-high degree of agreement indicates that photogrammetric models generated in RealityCapture can provide reasonably accurate RQD estimations.

Physical Vs 3DGS

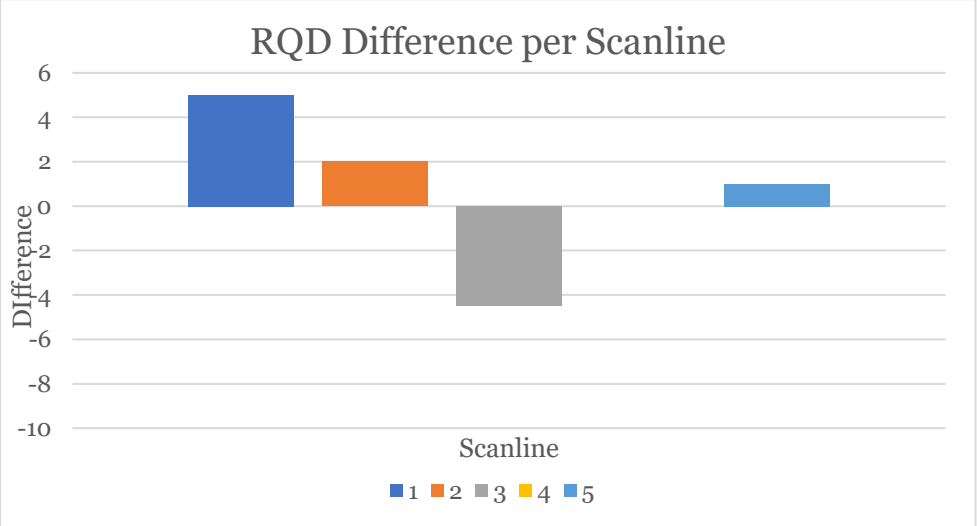

Figure 25: shows the RQD difference between the physical measurements and the 3DGS model measurements in a bar chart

A correlation plot was generated between the physical RQD values and the values obtained from the Gaussian splatting model, A 1:1 line was added to show the perfect agreement. The data showed a moderate positive correlation ($R^2 \approx 0.61$), indicating that the 3DGS closely followed the trend of the physically measured values, with minor deviations likely arising from reconstruction noise and joint delineation uncertainties in the 3D model.

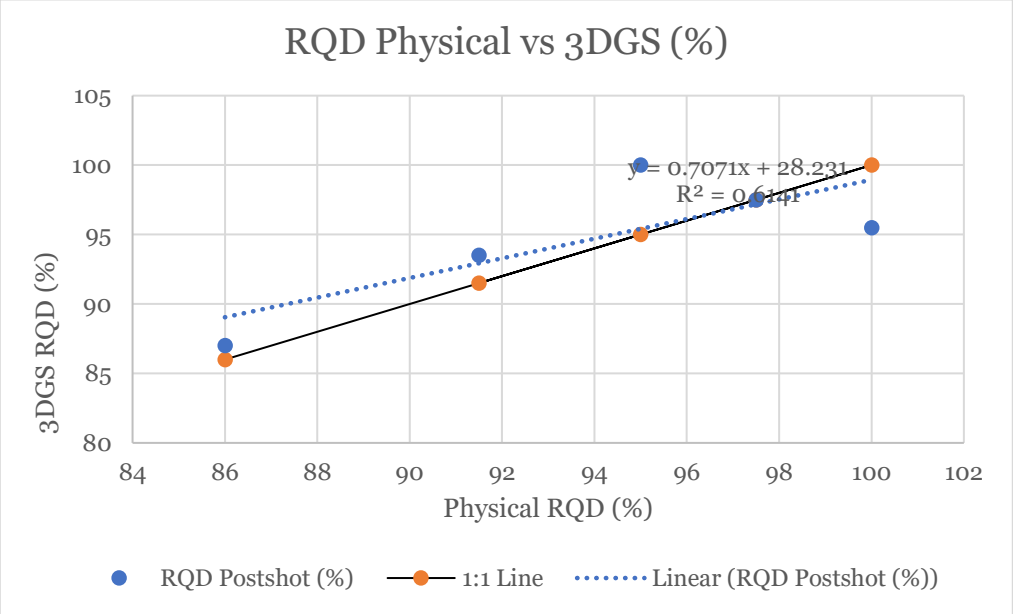

Figure 26: shows the correlation graph of RQD measurements between the 3DGS model measurements and the physical measurements. The orange dots indicate the 1:1 correlation, if the scanlines were all perfectly correlated, what was supposed to be observed. The blue dots on the other hand indicate the actual correlation points between the manual and 3DGS for every scanline, with the blue dotted lines showing the trendline of the actual correlation.

The data set showed a strong positive correlation with a Pearson correlation coefficient: r = 0.78364. The mean absolute error across the five scanlines is 2.5% and the mean RQD values are nearly identical: Physical = 94%, 3DGS = 94.7%.

The RQD measured from the Postshot processed model which was measured in 3D Vista Tour Pro to represent the 3D gaussian splatting measurements was compared to the physical RQD measurements in table 5, and showed differences as low as 0% in the scanline 4 and as high as 5% in the scanline 1. These individual discrepancies likely reflect local reconstruction differences (occlusion, small fractures missed or merged in the model) rather than a general bias. The regression fit yielded $R^2 \approx 0.61$, meaning about 61% of the variance in the 3DGS model value is explained by the physical measurements. However, the correlation p-value ($p=0.117$) is not below the standard 0.05 threshold, which was expected given the small sample size ($n=5$). With differences ranging from ±9% in RealityCapture to ±5% in Postshot, the RQD values derived from RealityCapture and Postshot displayed trends that were comparable to the physical measurements across all scanlines.

Overall, the average RQD for all scanlines was 91.2% for RealityCapture, 94.7% for Postshot, and 94% for the physical measures. The digital methods showed quite strong correlation to the field values in the mean RQD, however

individual scanlines showed discrepancies of up to 9% in the photogrammetric model measurements and 5% in the 3DGS measurements.

While the 3DGS model produced identical or marginally higher results in many circumstances (such as in Scanline 1), the photogrammetric model produced marginally lower results in most circumstances (such as scanline 3). The digital methods are seen to generally understate or overstate RQD when compared to the physical measurements.

For these measurements, the 3DGS measurements showed better RQD correlations to the physical measurements than the photogrammetric measurements. The small sample size and the existence of outliers in the scanline measurements warrants further testing on a larger dataset to confirm statistical significance to identify causes of the local discrepancies

Figure 27. Correlation heatmap for the different methods

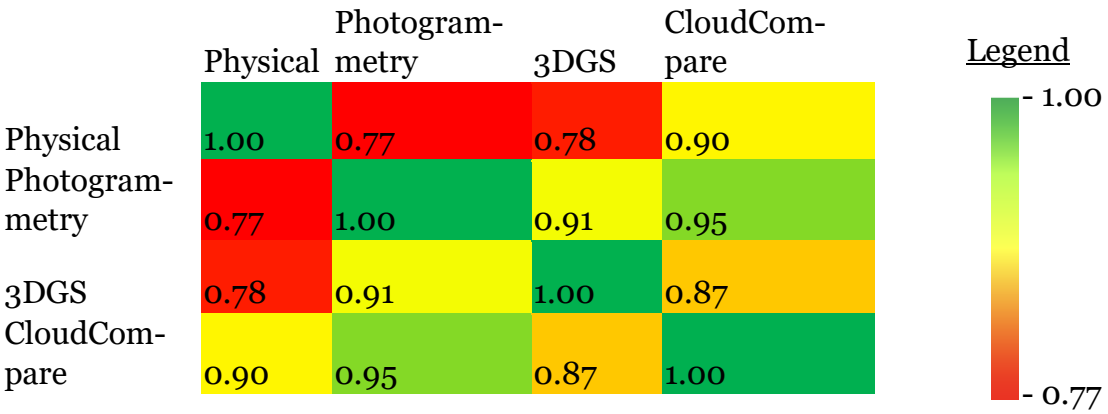

CloudCompare showed the strongest correlation with Photogrammetry (r = 0.9495), both are photogrammetric methods. CloudCompare also showed a stronger correlation with the Physical measurements (r = 0.8980).

Photogrammetry and 3DGS correlate strongly (r = 0.9065), indicating high agreement between the two digital reconstruction methods despite their different internal representations (mesh vs. splats).

Physical vs 3DGS (r = 0.7836) and Physical vs RealityCapture (r = 0.7685) show moderate-to-strong agreement: both digital methods track the physical RQD trend reasonably well, though the 3DGS method slightly correlated more than the Photogrammetric method.

The diagonal = 1.0 of course indicates perfect self-correlation.

4.4.1 CloudCompare

CloudCompare was used primarily to assess how the digital RQD measurements derived from the Gaussian Splatting (Postshot) and photogrammetric

(RealityCapture) methods compared to measurements taken directly on the point cloud data. This comparison was intended to determine which digital reconstruction approach better preserved the geometric integrity of the rock surface when analyzed for discontinuity characteristics. The physical RQD values were not emphasized in this analysis, given their close agreement with the CloudCompare results, which served as the baseline reference for accuracy.

Table 6. Root mean square error table comparing the error differences in RQD between methods with CloudCompare RQD results. (CC = CloudCompare, Phy = Physical, RC = RealityCapture, Po = Postshot, SoD = Square of Difference)

Scanline	CC	RQD Phy	SoD (Phy-CC)	RQD RC	SoD (CC-RC)	RQD Po	SoD (CC-P)
1	95.5	95	0.3	96	0.3	100.0	20.3
2	92.5	91.5	1.0	87.5	25.0	93.5	1.0
3	96.0	100	16.0	91	25.0	95.5	0.3
4	100.0	97.5	6.3	100	0.0	97.5	6.3
5	86.0	86	0.0	81.5	20.3	87.0	1.0
Mean of Diff			4.70		14.10		5.75
RMSE			2.167948		3.754997		2.397916

The Root Mean Square Error (RMSE) analysis was used to evaluate the numerical accuracy of the digital RQD measurements against the CloudCompare reference values. Postshot (3D Gaussian Splatting) dataset produced an RMSE of 2.40, while the RealityCapture (photogrammetric) dataset yielded a higher RMSE of 3.86.

The values of the RMSE of the digital methods signifies that the Gaussian splatting method more closely estimates the point-cloud-derived measurements, suggesting higher geometric consistency and reduced distortion in discontinuity representation. The lower RMSE supports the observation that splat-based models retain local rock mass structure more effectively than textured mesh reconstructions. Also, the root mean square error of the physical measurements in reference to the CloudCompare measurements was understandably the lowest, reinforcing the justifications for (Fatolahzadeh & Sepúlveda, 2025; Panayotova et al., 2021) in using point-cloud based measuring software for making RQD measurements.

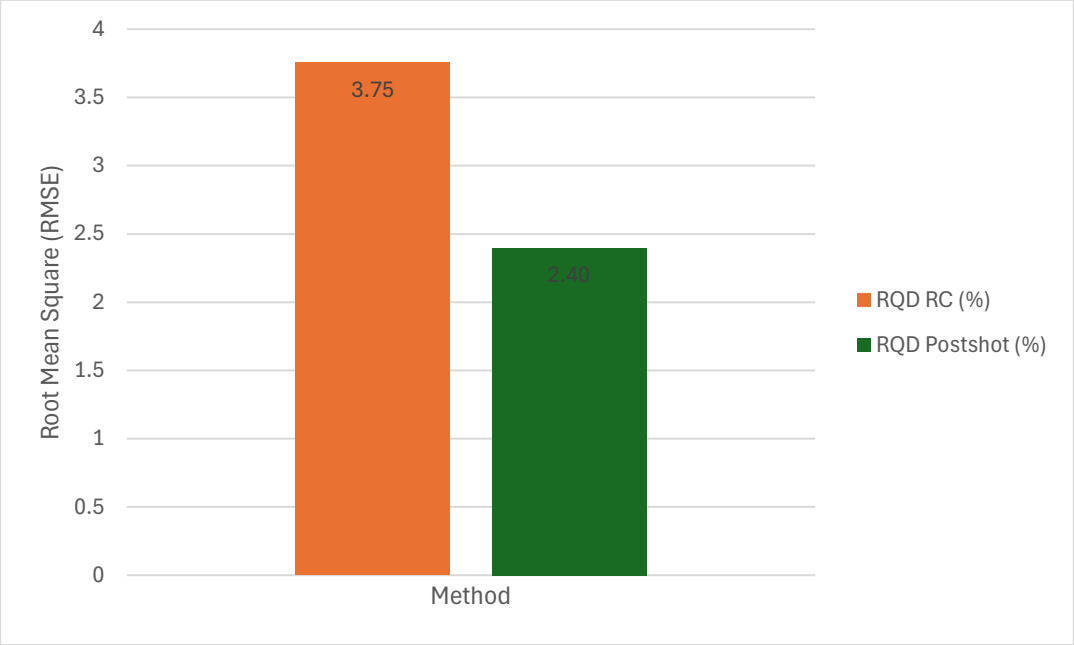

Figure 28. The root mean square error for the different digital methods using cloud compare as a reference method

4.5 Comparison between the visual quality of the phone generated model and the desktop generated model.

Figure 29 : Desktop generated 3DGS model with the Supersplat software

Figure 30 : Phone generated 3DGS model with the Supersplat software

To evaluate how device capabilities influenced the visual and metrical performance of 3D Gaussian Splatting (3DGS), the same tunnel image dataset was processed using the Supersplat web-based platform on both a mobile phone and a desktop computer. Supersplat was specifically chosen for this comparison because, unlike other 3DGS tools that operate exclusively

either on desktop or on mobile, its browser-based architecture allows the exact same software environment to run across different devices. This ensured that any possisble discrepancy observed would not be caused by inconsistent software but rather by hardware capabilities.

The visual comparison showed that both the mobile-generated and desktop-generated splat models exhibited a high-quality appearance. Key attributes such as fine-scale detail, lighting response, completeness of the scene, and the distinctive 3DGS view-dependent reflectance were consistently preserved across both devices. From a visualization standpoint, the mobile model proved fully capable of delivering accurate and immersive representations of the rock mass.

However, differences emerged in the measurement workflow. While the desktop model allowed sufficient zooming, stability, and control to pick individual splats for precise distance measurements, the mobile interface was noticeably restricted. The smaller screen size and limited zoom granularity prevented the user from reliably selecting specific splats, which is essential for high accuracy engineering measurements. This limitation did not affect visual interpretation but had a significant impact on metrical precision.

The comparison showed that although smartphones can generate visually robust 3DGS models suitable for rapid visualization and qualitative assessment, desktop-based systems remain superior for quantitative applications. The enhanced control, larger display area, and more precise interaction tools available on desktop environments make them more reliable for conducting accurate measurements required for rock engineering analysis.

5 CONCLUSIONS

This research demonstrates that 3D Gaussian Splatting (3DGS) holds significant potential as a feasible method for rock mass characterization. The findings in the thesis verify that 3DGS can fairly be employed as a quantitative tool for measuring key rock mass parameters, combining visual fidelity and geometric reliability within a single framework.

In this study, generating high-quality Gaussian splats in underground tunnel environments depended on adopting a data acquisition workflow similar to structure-from-motion photogrammetry. High resolution images, correct camera angles, stable camera motion, and careful exposure control were very essential in the low-light, high-contrast environment. Reliable splats further required optimized training parameters aligned with input data quality and GPU limitations, as well as post processing steps to remove floaters and noise. Together, these components defined an effective and replicable workflow for producing 3DGS models suitable for rock engineering application.

When compared to traditional photogrammetry-based methods, 3D Gaussian Splatting produced models with higher measurement precision and lower computational overhead. The comparative analysis between digital and physical Rock Quality Designation (RQD) measurements further validated these results: models generated through Gaussian Splatting (via Postshot) exhibited strong agreement with both physical reference measurements and point cloud–based reference datasets processed in CloudCompare. This proves that 3DGS achieves good metrical accuracy comparable to already established techniques while maintaining efficiency in data processing and visualization.

The research also showed that the measurement process in 3D Gaussian Splatting closely parallels the approach used in point-cloud-based methods, in that both derive spatial information from specific points in three-dimensional space rather than texture data. However, this also raises an important methodological question regarding the spatial origin of measurements on splat surfaces and how overlapping splats may influence the precision and repeatability of these measurements. Addressing this question represents a critical step toward establishing 3DGS as a standardized metrical tool in geotechnical modelling.

The tests across multiple 3DGS processing toolchains also showed that geometric distance measurements remain broadly consistent. While minor fluctuations which were mostly due to differences in the number of significant figures used by the different software platforms were observed, the underlying 3D geometry was consistent across all software platforms, supporting the technical soundness of 3DGS for metrical analysis.

While the workflow with the personal computer produced denser and more stable reconstructions, smartphone-based 3DGS demonstrated strong

potential for rapid, low-cost field documentation, especially where speed and accessibility are prioritized over the highest possible accuracy.

Future work could therefore focus on characterizing the spatial behaviour of splat overlaps and their influence on geometric accuracy. One promising direction involves conducting controlled experiments comparing localized point clouds with 3DGS-derived area measurements at micro scales, to precisely trace where on the splat surface measurement points are defined. Additionally, expanding the application of this method to rock masses with very poor RQD values could provide a broader validation of its robustness across different geological conditions. These next steps could deepen the understanding of 3DGS measurement process and strengthen its position as an innovative, accurate, and efficient approach for digital rock mass characterization.

6 References

Balabanian, A. (2024, July 21). *RealityCapture to Gaussian Splatting using PostShot – Azad's Blog*. https://azadux.blog/2024/07/21/realitycaptureto postshot/

Baqersad, J., Poozesh, P., Niezrecki, C., & Avitabile, P. (2017). *Photogrammetry and optical methods in structural dynamics – A review Author links open overlay panel. 86*, 17–34. https://doi.org/10.3390/min11060585

Bscan. (2013, March 22). *File:MultivariateNormal.png - Wikimedia Commons*. https://commons.wikimedia.org/wiki/File:MultivariateNormal.png

Calantropio, A., & Chiabrando, F. (2024). Underwater Cultural Heritage Documentation Using Photogrammetry. In *Journal of Marine Science and Engineering* (Vol. 12, Issue 3). Multidisciplinary Digital Publishing Institute (MDPI). https://doi.org/10.3390/jmse12030413

Chan, K. C., Xiao, J., Goshu, H. L., & Lam, K. M. (2024). Point Cloud Densification for 3D Gaussian Splatting from Sparse Input Views. *MM 2024 - Proceedings of the 32nd ACM International Conference on Multimedia*, 896–904. https://doi.org/10.1145/3664647.3681454

Chen, G., & Wang, W. (2025). A Survey on 3D Gaussian Splatting. *IEEE TRANSACTIONS ON PATTERN ANALYSIS AND MACHINE INTELLIGENCE*. https://github.com/guikunchen/Awesome3DGS

Chen, J., Fang, Q., Zhang, D., & Huang, H. (2023). A critical review of automated extraction of rock mass parameters using 3D point cloud data. In *Intelligent Transportation Infrastructure* (Vol. 2). Oxford University Press. https://doi.org/10.1093/iti/liad005

Cheng, K., Long, X., Yang, K., Yao, Y., Yin, W., Ma, Y., Wang, W., & Chen, X. (2024). *GaussianPro: 3D Gaussian Splatting with Progressive Propagation*. https://github.

Cicilie Trede1, Nestor Cardozo1, & Lisa Watson1. (2019). What is the appropriate sample size for strike and dip measurements? An evaluation from compass, smartphone and LiDAR measurements. *NORWEGIAN JOURNAL OF GEOLOGY*.

Davide, C., Simone, M., & Giovanna, P. (2023). *View of Aerial photogrammetry used as a quick procedure for rock mass stability analysis in a nature reserve*. Italian Journal of Engineering Geology and Environment . https://rosa.uniroma1.it/rosa02/engineering_geology_environment/article/view/1512/1369

Deere D.U. (1964). *D. U. Deere, "Technical Description of Rock Cores for Engineering Purpose," Rock Mechanics and Engineering Geology, Vol. 1, No. 1, 1963, pp. 16-22. - References - Scientific Research Publishing*. https://www.scirp.org/reference/referencespapers?referenceid=974800

Deheng Kong, Charalampos Saroglou, Faquan Wu, Peng Sha, & Bo Li. (2021). Development and application of UAV-SfM photogrammetry for quantitative characterization of rock mass discontinuities Author links open overlay panel. *International Journal of Rock Mechanics and Mining Sciences* , *141*. https://doi.org/10.3390/min11060585

Deliry, S. I., & Avdan, U. (2021). Accuracy of Unmanned Aerial Systems Photogrammetry and Structure from Motion in Surveying and Mapping: A Review. In *Journal of the Indian Society of Remote Sensing* (Vol. 49, Issue 8, pp. 1997–2017). Springer. https://doi.org/10.1007/s12524-021-01366-x

Fatolahzadeh, S., & Sepúlveda, S. A. (2025). Comparison between Two New Ground-Based Remote Sensing Techniques for Rock Mass Characterization. *Canadian Journal of Remote Sensing*, *51*(1). https://doi.org/10.1080/07038992.2025.2470710;WEBSITE:WEBSITE:TFOPB;PAGEGROUP:STRING:PUBLICATION

Fei, B., Xu, J., Zhang, R., Zhou, Q., Yang, W., & He, Y. (2024). 3D Gaussian Splatting as New Era: A Survey. *IEEE Transactions on Visualization and Computer Graphics*. https://doi.org/10.1109/TVCG.2024.3397828

Geppert, M., Larsson, V., Speciale, P., Schönberger, J. L., & Pollefeys, M. (2020). *Privacy Preserving Structure-from-Motion* (A. Vedaldi, H. Bischof, T. Brox, & J.-M. Frahm, Eds.; Vol. 12346). Springer International Publishing. https://doi.org/10.1007/978-3-030-58452-8

Gottron, D., & Henk, A. (2021). Upscaling of fractured rock mass properties – An example comparing Discrete Fracture Network (DFN) modeling and empirical relations based on engineering rock mass classifications. *Engineering Geology*, *294*. https://doi.org/10.1016/j.enggeo.2021.106382

Herrero, M. J., Pérez-Fortes, A. P., Escavy, J. I., Insua-Arévalo, J. M., De la Horra, R., López-Acevedo, F., & Trigos, L. (2022). 3D model generated from UAV photogrammetry and semi-automated rock mass characterization. *Computers and Geosciences*, *163*. https://doi.org/10.1016/j.cageo.2022.105121

Janiszewski, M., Prittinen, M., Uotinen, L., Torkan, M., & Rinne, M. (2023). *Rapid photogrammetric method for rock mass characterization in underground excavations*. 213–221. https://doi.org/10.33112/nrock2023.20

Janiszewski, M., Torkan, M., Uotinen, L., & Rinne, M. (2022). Rapid Photogrammetry with a 360-Degree Camera for Tunnel Mapping. *Remote Sensing*, *14*(21). https://doi.org/10.3390/rs14215494

Kerbl, B., Kopanas, G., Leimkuehler, T., & Drettakis, G. (2023). 3D Gaussian Splatting for Real-Time Radiance Field Rendering. *ACM Transactions on Graphics*, *42*(4). https://doi.org/10.1145/3592433

Kimberly Schulte. (2021). *Geologic Tools*. Lumen Learning. https://doi.org/10.3390/min11060585

Kissi-Ameyaw, J., Mcisaac, K., Wang, X., & Osinski, G. R. (2020). *Towards an Automatic System for Extracting Planar Orientations from Software Generated Point Clouds*.

Kumar Singh, S., Pratap Banerjee, B., & Raval, S. (2023). A review of laser scanning for geological and geotechnical applications in underground mining. In *International Journal of Mining Science and Technology* (Vol. 33, Issue 2, pp. 133–154). China University of Mining and Technology. https://doi.org/10.1016/j.ijmst.2022.09.022

Meng, J., Li, H., Wu, Y., Gao, Q., Yang, S., Zhang, J., & Ma, S. (2024). *Mirror-3DGS: Incorporating Mirror Reflections into 3D Gaussian Splatting*. http://arxiv.org/abs/2404.01168

Mildenhall, B., Srinivasan, P. P., Tancik, M., Barron, J. T., Ramamoorthi, R., & Ng, R. (2020). *NeRF: Representing Scenes as Neural Radiance Fields for View Synthesis*. http://arxiv.org/abs/2003.08934

Niantic Spatial. (2021). *Scaniverse: 3D Scanning App | Niantic Spatial, Inc.* https://www.nianticspatial.com/en/products/scaniverse

Panayotova, M., DSc Vladimir, A., Carsten Drebenstedt -TU Bergakademie Freiberg, hc, DSc Vladimir, G., Vladimir, Ds., & Stefan Dimovski, Ds. (2021). Application of photogrammetry for determination of volumetric joint count as a measure for improved Rock Quality Designation (RQD) index. *Sustainable Extraction and Processing of Raw Materials Journal*. http://www.mgu.bgwww.seprm.com©

PlayCanvas. (2025). *SuperSplat* (2.10.0). https://superspl.at/editor/

Rangel-Buitrago, N., Galgani, F., Nicoll, K., & Neal, W. J. (2024). Rethinking geological concepts in the age of plastic pollution. *Science of The Total Environment*, *950*, 175366. https://doi.org/10.1016/J.SCITOTENV.2024.175366

Remondino, F., Karami, A., Yan, Z., Mazzacca, G., Rigon, S., & Qin, R. (2023). A Critical Analysis of NeRF-Based 3D Reconstruction. *Remote Sensing*, *15*(14). https://doi.org/10.3390/rs15143585

Schönberger, J. L., & Frahm, J.-M. (2016). *Structure-from-Motion Revisited*. https://github.com/colmap/colmap.

Steven Earle. (2019). *Physical Geology* (Second Edition). https://doi.org/10.3390/min11060585

Sultan Shah, K., Hazizan bin Mohd Hashim, M., & Shah bin Ariffin, K. (2022). Photogrammetry and Monte Carlo Simulation based statistical characterization of rock mass discontinuity parameters. *International Journal of Mining and Geo-Engineering*. https://doi.org/10.22059/IJMGE.2021.310570.594866

Thambidurai N Singh, P. T. (2023). *Landslides: Detection, Prediction and Monitoring Technological Developments*.

Tosi, F., Zhang, Y., Gong, Z., Sandström, E., Mattoccia, S., Oswald, M. R., & Poggi, M. (2024). *How NeRFs and 3D Gaussian Splatting are Reshaping SLAM: a Survey*. http://arxiv.org/abs/2402.13255

Ullman, S. (1979). The interpretation of structure from motion. *Proc. R. Soc. Lond. B*, *203*, 405–426. https://royalsocietypublishing.org/

Wu, T., Yuan, Y.-J., Zhang, L.-X., Yang, J., Cao, Y.-P., Yan, L.-Q., Gao, L., & Author, T. (2024). *Computational Visual Media Recent advances in 3D Gaussian splatting*. *10*(4), 613–642. https://doi.org/10.1007/s41095-024-0436-y

Yazarı, Y., Mühendisliği Dergisi, J., Çağlardan Günümüze Yer Altı Yapıları, İ., Yapıları ve Kaya Mekaniği Ebru AKIŞ, K., & Satici, Ö. (2017). Underground Structures, Rock Structures and Rock Mechanics from Ancient Era to the Modern Age. *Journal of Geological Engineering*, *41*, 155–172. https://doi.org/10.24232/jmd.344499

APPENDICES

Appendix A – Leica laser meter measurements for the manual distance measurements

Table 7. Physical measurements in the tunnel with the laser meter (in meters)

	1	2	3	4	5	MEAN	STANDARD DEVIATION
SHORT	0.1058	0.1076	0.1079	0.1063	0.1058	0.10667623	0.00089755
MEDIUM	1.5301	1.5336	1.5339	1.5286	1.5319	1.53161865	0.00203116
LONG	2.9557	2.9521	2.9382	2.9484	2.9469	2.94825412	0.0058851

Five different distance measurements were made with the laser meter for each defined distance (short, medium or long). The mean of these distances was computed to represent the physical distance measurements.

Appendix B – The RQD measurements from the three different methods considering the segments from all five (5) scanlines

Table 8. The difference in segment properties of the Physical, Photogrammetric and 3DGS in the RQD measurements

Physical Measurements				**Photogrammetric measurements**				**3D Gaussian splatting measurements**			
Scanline 1				**Scanline 1**				**Scanline 1**			
Seg-ment	Start	End	Length	Seg-ment	Start	End	Length	Segment	Start	End	Length
1	0	0.28	0.28	1	0	0.27	0.27	1	0	0,27	0,27
2	0.28	0.42	0.14	2	0.27	0.41	0.14	2	0,27	0,41	0,14
3	0.42	0.48	0.06	3	0.41	0.49	0.08	3	0,41	0,51	0,1
4	0.48	0.52	0.04	4	0.49	0,052778	0.27	4	0,51	1,58	1,07
5	0.52	0,084028	1.09	5	0,052778	1.52	0,052778	5	1,58	1,75	0,17
6	0,084028	1.08	0.19	6	1.52	0,094444	0.24	6	1,75	2	0,25
7	1.08	2	0.02	7	0,094444	2	0.24				
RQD			95	RQD			96	RQD			100
Scanline 2				**Scanline 2**				**Scanline 2**			
Seg-ment	Start	End	Length	Seg-ment	Start	End	Length	Segment	Start	End	Length
1	0	0.06	0.06	1	0	0.08	0.08	1	0	0,06	0,06
2	0.06	0.09	0.03	2	0.08	0.11	0.03	2	0,06	0,11	0,05
3	0.09	0.17	0.08	3	0.11	0.17	0.06	3	0,11	0,21	0,1
4	0.17	0.34	0.17	4	0.17	0.36	0.19	4	0,21	0,4	0,19

5	0.34	0.51	0.17
6	0.51	0,047917	0.18
7	0,047917	0,060417	0.18
8	0,060417	0,085417	0,052778
9	0,085417	2	0.37
RQD			91.05.00

5	0.36	0,045139	0.29
6	0,045139	0,050694	0.08
7	0,050694	0,063889	0.19
8	0,063889	1.26	0.34
9	1.26	0,086111	0.38
10	0,086111	2	0.36
RQD			87.05.00

5	0,4	0,65	0,25
6	0,65	0,67	0,02
7	0,67	0,85	0,18
8	0,85	1,42	0,57
9	1,42	2	0,58
RQD			93,5

Scanline 3

Seg-ment	Start	End	Length
1	0	0.29	0.29
2	0.29	0.43	0.14
3	0.43	0.56	0.13
4	0.56	0,047917	0.13
5	0,047917	0,056944	0.13
6	0,056944	0,09375	0,064583
7	0,09375	2	0.25
RQD			100

Scanline 3

Seg-ment	Start	End	Length
1	0	0.23	0.23
2	0.23	0.39	0.16
3	0.39	0.48	0.09
4	0.48	0.57	0.09
5	0.57	0,046528	0.01
6	0,046528	0.08	0.13
7	0.08	1.12	0.32
8	1.12	2	0,061111
RQD			91

Scanline 3

Segment	Start	End	Length
1	0	0,26	0,26
2	0,26	0,42	0,16
3	0,42	0,51	0,09
4	0,51	0,72	0,21
5	0,72	1,36	0,64
6	1,36	1,63	0,27
7	1,63	2	0,37
RQD			95,5

Scanline 4

Seg-ment	Start	End	Length
1	0	0.22	0.22

Scanline 4

Seg-ment	Start	End	Length
1	0	0.24	0.24

Scanline 4

Segment	Start	End	Length
1	0	0,21	0,21

2	0.22	0.43	0.21
3	0.43	0.55	0.12
4	0.55	0.06	0.05
5	0.06	1.36	0,052778
6	1.36	2	0,044444
RQD			97.05.00

2	0.24	0.45	0.21
3	0.45	0.57	0.12
4	0.57	0,047917	0.12
5	0,047917	1.34	0,045139
6	1.34	2	0,045833
RQD			100

2	0,21	0,43	0,22
3	0,43	0,48	0,05
4	0,48	0,7	0,22
5	0,7	0,81	0,11
6	0,81	1,59	0,78
7	1,59	2	0,41
RQD			97,5

Scanline 5

Seg-ment	Start	End	Length
1	0	0.12	0.12
2	0.12	0.16	0.04
3	0.16	0.29	0.13
4	0.29	0.36	0.07
5	0.36	0.05	0.14
6	0.05	1.58	1.08
7	1.58	0,088194	0.09
8	0,088194	0,096528	0.12
9	0,096528	0,099306	0.04
10	0,099306	0,102083	0.04
11	0,102083	2	0.13
RQD			86

Scanline 5

Seg-ment	Start	End	Length
1	0	0.05	0.05
2	0.05	0.13	0.08
3	0.13	0.38	0.25
4	0.38	1.37	0,06875
5	1.37	1.52	0.15
6	1.52	0,084722	0.01
7	0,084722	0,090972	0.09
8	0,090972	1.08	0.09
9	1.08	0,101389	0.06
10	0,101389	2	0.14
RQD			81.05.00

Scanline 5

Segment	Start	End	Length
1	0	0,06	0,06
2	0,06	0,13	0,07
3	0,13	0,39	0,26
4	0,39	1,36	0,97
5	1,36	1,52	0,16
6	1,52	1,63	0,11
7	1,63	1,72	0,09
8	1,72	1,83	0,11
9	1,83	1,87	0,04
10	1,87	2	0,13
RQD			87

Appendix C – The RQD measurements made from the point clouds considering the individual scanlines made in Cloud-Compare software.

Figure 31. CloudCompare RQD results

Scanline 1			
Segment	Start	End	Length
1	0	0.29	0.29
2	0.29	0.41	0.12
3	0.41	0.5	0.09
4	0.5	0.76	0.26
5	0.76	1.51	0.75
6	1.51	1.73	0.22
7	1.73	2	0.27
RQD			95.5

Scanline 2			
Segment	Start	End	Length
1	0	0.06	0.06
2	0.06	0.08	0.02
3	0.08	0.18	0.1
4	0.18	0.33	0.15
5	0.33	0.62	0.29
6	0.62	0.69	0.07
7	0.69	0.9	0.21
8	0.9	1.24	0.34
9	1.24	2	0.76
RQD			92.5

Scanline 3			
Segment	Start	End	Length
1	0	0.24	0.24
2	0.24	0.59	0.35
3	0.59	0.67	0.08
4	0.67	0.85	0.18
5	0.85	1.02	0.17
6	1.02	1.19	0.17
7	1.19	1.65	0.46
8	1.65	2	0.35

RQD			96

Scanline 4

Segment	Start	End	Length
1	0	0.27	0.27
2	0.27	0.47	0.2
3	0.47	0.65	0.18
4	0.65	0.83	0.18
5	0.83	1.75	0.92
6	1.75	2	0.25
RQD			100

Scanline 5

Segment	Start	End	Length
1	0	0.05	0.05
2	0.05	0.12	0.07
3	0.12	0.18	0.06
4	0.18	0.37	0.19
5	0.37	1.37	1
6	1.37	1.61	0.24
7	1.61	1.77	0.16
8	1.77	1.84	0.07
9	1.84	1.87	0.03
10	1.87	2	0.13
RQD			86